Research Square

Preprints are preliminary reports that have not undergone peer review.
They should not be considered conclusive, used to inform clinical practice,
or referenced by the media as validated information.

IGF1R trafficking is modulated by VPS25/ESCRT-II in mice and humans to control skeletal fate commitment

Licia Selleri

Licia.Selleri@ucsf.edu

University of California San Francisco (UCSF) https://orcid.org/0000-0002-6817-1469

Viviana Hermosilla Aguayo

University of California, San Francisco (UCSF) https://orcid.org/0000-0002-2495-4867

Maurizio Risolino

University of California, San Francisco (UCSF)

Jaiden de Anda

University of California, San Francisco (UCSF)

Mais Hashem

Department of Translational Genomics, Center for Genomic Medicine, King Faisal Specialist Hospital and Research Center

Samya Habeeb

Saudi Germany Hospital

Lama AlAbdi

King Faisal Specialist Hospital and Research Center, Riyadh

Article

Keywords:

Posted Date: November 2nd, 2026

DOI: https://doi.org/10.21203/rs.3.rs-11504315/v1

License: This work is licensed under a Creative Commons Attribution 4.0 International License.
Read Full License

Additional Declarations: There is **NO** Competing Interest.

IGF1R trafficking is modulated by VPS25/ESCRT-II in mice and humans to control skeletal fate commitment

Viviana Hermosilla-Aguayo[1,2,3]*, Jaiden de Anda[1,2,3], Maurizio Risolino[1,2,3], Mais O. Hashem[4], Samya Habeeb[5], Lama AlAbdi[4], and Licia Selleri[1,2,3,6,7]*.

[1] Program in Craniofacial Biology, University of California, San Francisco, San Francisco, CA 94143, USA.

[2] Department of Orofacial Sciences, University of California, San Francisco, San Francisco, CA 94143, USA.

[3] Department of Anatomy, University of California, San Francisco, San Francisco, CA 94143, USA.

[4] Department of Translational Genomics, King Faisal Specialist Hospital and Research Center, Riyadh, Saudi Arabia.

[5] Pediatric Intensive Care Unit, Saudi Germany Hospital, Dammam, Saudi Arabia.

[6] Institute for Human Genetics, University of California, San Francisco, San Francisco, CA 94143, USA.

[7] Eli and Edythe Broad Center of Regeneration Medicine & Stem Cell Research, University of California, San Francisco, San Francisco, CA 94143, USA.

*Co-corresponding authors:

Viviana Hermosilla Aguayo (Viviana.HermosillaAguayo@ucsf.edu)

Licia Selleri (Licia.Selleri@ucsf.edu)

ABSTRACT

Cranial neural crest cell (CNCC)-derived osteochondroprogenitors commit to either bone or cartilage by fine-tuning master transcription factors. However, it remains unclear how extracellular cues regulate this critical cell fate decision. Here, we show that loss of VPS25, an ESCRT-II subunit required for lysosomal degradation of activated membrane receptors, impairs ossification in mouse embryos and CNCC-derived cells. VPS25 loss reduces osteogenesis, while upregulating early and late chondrogenic markers *in vitro*, even under cell culture osteogenic induction. In *Vps25* mutant mice, the shift toward cartilage at the expense of bone precedes early chondrogenesis, indicating skewed osteochondroprogenitor fate. Mechanistically, VPS25 loss causes endosomal accumulation of activated insulin-like growth factor 1 receptor (IGF1R) in mutant murine cells and in fibroblasts from patients with biallelic *VPS25* variants associated with a fatal congenital developmental syndrome. Pharmacological IGF1R inhibition rescues lineage identity in mutant craniofacial skeletal tissues *in vivo* and in mutant cultured cells. These findings reveal a previously unrecognized role for ESCRT-II in controlling skeletal fate through IGF signaling, providing new mechanistic insight into skeletal cell fate determination and pointing to IGF1R modulation as a potential avenue for mitigating human craniofacial abnormalities.

INTRODUCTION

The skeletal system comprises bones, cartilage, tendons, and ligaments that provide structural support and allow for movement[1–3]. Importantly, both bone and cartilage derive from the same mesenchymal progenitors that commit to either lineage based on finely-tuned levels of master transcription factors[2,4–6]. Bipotential osteochondroprogenitors co-express transcription factor-encoding genes *Sox9* and *Runx2*[2,4]. SOX9 initiates chondrocyte fate commitment by driving the expression of *Col2a2* (type II collagen) and *Acan* (Aggrecan), while inhibiting RUNX2 function[2,7–9]. The osteoblast lineage is specified by RUNX2-driven expression of *Sp7* (Osterix), followed by expression of *Col1a1* (type I collagen), *Bglap* (osteocalcin), and *Spp1* (osteopontin) [2,6,10–12]. Abnormal bone shape, size, and composition underlie pathologies including dysplasias (e.g., achondroplasia), metabolic bone disorders (e.g., rickets), and congenital abnormalities, many affecting the craniofacial complex (e.g., orofacial clefts and micrognathia) in mice and humans[13–19]. Craniofacial reconstructive surgery is needed to treat congenital anomalies such as cleft lip and/or palate[20–22] -affecting 1 in every 700 births[21,23]-, and also conditions such as trauma, or oncologic resection[22,24,25]. Head reconstructive surgeries pose multiple challenges, as they require restoring intricate skeletal architecture[26,27]. Accordingly, deeper insight into the mechanisms of craniofacial bone morphogenesis is needed to design novel therapeutic strategies for reconstruction and/or regeneration of cranial bones[26,28].

In the mammalian craniofacial complex, the majority of the skeletal components derive from Cranial Neural Crest Cells (CNCC), a migratory multipotent cell population that differentiates into bone and cartilage, among other lineages[4]. Multiple signaling pathways are critical for the proper development and growth of facial cartilage and bone [4,29]. To attenuate signaling pathways, cells endocytose and sort ligand-activated receptors into lysosomes for degradation[30,31], which requires an evolutionarily conserved protein machinery known as ESCRT (Endosomal Sorting Complexes Required for Transport)[30,32,33]. The ESCRT machinery comprises five protein complexes (ESCRT-0, ESCRT-I, ESCRT-II, ESCRT-III, and VPS4) sequentially recruited to cellular membranes[33–36]. While the biochemical and cellular physiology of the ESCRT

machinery has been widely studied *in vitro* or in invertebrate animal models[37–41], its roles in vertebrate embryonic development are not yet fully understood due to early embryonic lethality of mouse mutants with ESCRT loss-of-function (LOF)[42–50].

We previously reported the isolation of a mouse hypomorphic allele for the ESCRT-II-encoding gene *Vps25*[46], hereafter referred to as *Vps25*^{ENU}. *Vps25*$^{ENU/ENU}$ mutant embryos displayed fully penetrant polydactyly[46], dilated brain ventricles, and thinned cerebral cortex[51]. In addition, they exhibited craniofacial defects including microcephaly, hypoplastic lower jaw, stunted snout, low-set ear pinnae, cleft of the secondary palate, and hollow temporal bone[46,52]. While constitutive *Vps25*-null mouse embryos die *in utero* before E8.5[46,53], *Vps25*$^{ENU/ENU}$ mutants display later lethality (E15.5 -E16.5), providing the first evidence for the roles of ESCRT-II in limb and craniofacial development [46,52]. In addition, *Vps25*$^{ENU/ENU}$ embryos, as well as embryos with *Vps25* mesenchymal-specific deletion, exhibit strikingly impaired bone formation. Here, we show that CNCC-derived craniofacial cells from mice with *Vps25* LOF are skewed towards chondrogenic lineage commitment at the expense of osteogenic differentiation using both *in vivo* and *in vitro* models. This phenotype is especially compelling in light of the recent report that the loss of ESCRT-III protein CHMP5 increases bone formation[54], highlighting potentially opposing roles for distinct ESCRT proteins in skeletal development.

We also uncover that *Vps25* LOF in murine head mesenchyme causes hyperactivation of the Insulin like Growth Factor (IGF) pathway. Furthermore, cultured murine cranial mesenchymal cells lacking *Vps25* exhibit enhanced chondrogenesis, with features resembling hypertrophic cartilage even under osteogenic induction. Mechanistically, in murine *Vps25* mutant mesenchymal cells, the IGF-1 receptor (IGF1R) is trapped and accumulates in late endosomes/lysosomes during *in vitro* osteogenic induction. Notably, IGF1R accumulation is also observed in primary fibroblasts from patients carrying biallelic *VPS25* variants associated with neonatal encephalopathy and craniofacial defects. Pharmacological inhibition of IGF1R restores both the receptor's intracellular localization and the osteogenic differentiation potential of murine *Vps25* mutant cells *in vitro,* while reducing chondrogenesis *in vitro* and in the craniofacial complex *in vivo.*

Collectively, our results uncover a new role for the ESCRT-II machinery in modulating skeletal fate commitment through IGF signaling and provide new mechanistic understanding of craniofacial skeletal morphogenesis.

RESULTS

VPS25 is required for palatal closure and bone formation in murine development.

We previously characterized the phenotype of embryos carrying a *Vps25* hypomorphic mutation, referred to as *Vps25*^{ENU}[46,52]. Unlike constitutive *Vps25* LOF, the *Vps25*^{ENU} homozygous hypomorphic mutation allows embryonic survival until gestational day 16.5 (E16.5)[46]. *Vps25*$^{ENU/ENU}$ embryos display fully penetrant polydactyly and drastic craniofacial defects that include microcephaly, stunted snout, hypoplastic lower jaw, low-set ear pinna, and secondary palatal cleft[46,52] (Supplementary Figure 1a). Further characterization by alizarin red staining revealed that multiple craniofacial bones are absent or hypoplastic in *Vps25*$^{ENU/ENU}$ mutant *versus* wild-type control embryos at E15.5 (Figure 1a). Importantly, upon *Vps25* LOF, impaired bone formation is also observed in long bones such as hindlimbs and forelimbs and axial skeleton (Supplementary Figure 1b). Trichrome RGB staining in coronal sections confirmed secondary palatal cleft due to impaired elevation of palatal shelves (Figure 1b). In addition, decreased dense collagen staining, indicative of early bone formation[55], was observed in the lower jaw of *Vps25* homozygous mutant embryos (Figure 1b, dark pink areas) compared to controls. Immunohistochemistry showed decreased levels of the bone marker ALPL[56] (alkaline phosphatase), in palatal shelves from E14.5 mutant compared to control embryos (Figure 1c). Similarly, levels of the master osteogenic transcription factors SP7[2,10] (Osterix, Figure 1d) and RUNX2[57] (Runt-Related Transcription Factor 2, Figure 1e), were decreased in upper and lower jaws of E14.5-E15.0 *Vps25*$^{ENU/ENU}$ compared to controls. Downregulated *Runx2* expression was detected as early as E12.5 in branchial arch 1 (BA1) mutant mesenchyme by qRT-PCR with specific primers directed to either the 5' or 3' *Runx2* transcript (Figure 1f). Lastly, defective osteogenic differentiation persisted until later stages, as ALPL and SP7 downregulation was still observed in

E15.5 mutant upper and lower jaws (Supplementary Figures 1c-d), prior to embryonic lethality. Altogether, our results report a previously unexplored, yet critical role, of the ESCRT-II machinery in murine bone formation.

VPS25 plays tissue-specific roles in the murine cephalic epithelium.

To identify which craniofacial tissues exhibit higher levels of VPS25, we conducted immunodetection and quantification of transcripts at early and mid-gestational stages (Figures 2a-c). VPS25 was present in both BA1 epithelium and mesenchyme of E9.5 wildtype embryos (Figure 2a), as seen by co-detection of the epithelial-specific marker EpCAM[58]. qRT-PCR quantification of *Vps25*, the epithelial genes *EpCam* and *Cdh1*, as well as the mesenchymal-specific gene *Hand2*[59], showed that *Vps25* was expressed at similar levels in both cephalic epithelium and mesenchyme at E11.5. Of note, *Vps25* transcript levels were drastically decreased in $Vps25^{ENU/ENU}$ epithelium and mesenchyme *versus* control tissue (Figure 2b). Similarly, VPS25 was detected in E13.5 wildtype palatal shelf epithelium and mesenchyme, as seen by immunohistochemistry on wildtype coronal sections (Figure 2c).

Palatal shelves are formed by CNCC-derived mesenchyme surrounded by a thin epithelial layer[60]. To dissect tissue-specific functions of *Vps25* in palatal closure and skeletal development, we generated a *Vps25* conditional allele in the mouse. To this end, exon 2 was flanked by two *loxP* sites in the *Vps25* gene using EasiCRISPR[61,62], allowing *Cre*-mediated excision with tissue-specific *Cre* deleter lines (Figure 2d). In $Crect^{Cre}$ carrier embryos[63], *Cre* activity has been reported in the early cephalic epithelium as well as the epithelia lining the oral cavity, including palatal shelves (PS)[58,64] (Supplementary Figure 2a). *CrectCre*-mediated *Vps25* homozygous LOF resulted in fully penetrant stunted snout and hypoplastic jaw as early as E12.5 (Supplementary Figures 2.b-c), resembling the phenotype observed in $Vps25^{ENU/ENU}$ hypomorphic embryos (Supplementary Figure 1.a). $Vps25^{fl/fl};Crect^{Cre/+}$ embryos also exhibited abnormal limb development (Supplementary Figure 2.b) and died *in utero* prior to secondary palatal fusion (E14.0). In addition, homozygous epithelial loss of

Vps25 led to abnormal palatal shelf growth (Supplementary Figure 2d). To further investigate cellular behaviors that could account for reduced growth of palatal shelves, we evaluated proliferation and apoptotic cell death by phospho-Histone H3 immunodetection and TUNEL staining, respectively (Supplementary Figure 2.e). While proliferation was not significantly affected by *Vps25* homozygous epithelial loss (Supplementary Figure 2.f), cell death was increased in *Vps25*$^{fl/fl}$*;Crect*$^{Cre/+}$ palatal epithelium and also in the mesenchyme compared to heterozygous controls (Supplementary Figure 2.g), indicating VPS25 cell-autonomous and non cell-autonomous roles in palatal cell survival.

VPS25 performs additional critical functions in the murine cephalic mesenchyme.

Next, we used a *Wnt1-Cre*^{Tg} deleter line[65] to inactivate *Vps25* in CNCC-derived mesenchyme. CNCC-specific homozygous *Vps25* loss caused earlier lethality (E11.5) associated with hemorrhagic hypoplastic BA1 and frontonasal processes (FNP, Supplementary Figure 3a). Using an *R26R*^{nTnG} reporter line[66], we showed that migration of CNCCs of the trigeminal stream that populate FNP and BA1 in E9.5 *Vps25*$^{fl/fl}$*;R26R*$^{nTnG/+}$*;Wnt1-Cre*$^{Tg/+}$ embryos was comparable to controls (Supplementary Figures 3b-c). However, trigeminal CNCCs underwent apoptosis by E10.5 in mutants, resulting in a strikingly hypoplastic trigeminal stream (Supplementary Figures 3d-e).

To circumvent early lethality caused by *Vps25* CNCC-specific inactivation, we crossed *Vps25*$^{fl/fl}$ embryos to *Shox2*$^{IRES-Cre}$ carriers[67] to remove *Vps25* from palatal mesenchyme (Figure 2e). We incorporated the *R26R*^{nTnG} reporter allele to visualize Cre+, GFP+ cells in specific craniofacial regions. Cre activity was detectable in limb mesenchyme as well as in the facial midline (Figure 2f). Accordingly, *Shox2*$^{IRES-Cre}$-mediated homozygous inactivation of *Vps25* caused fully penetrant cleft face with hypoplastic lower jaw, edema, and limb abnormalities (Figures 2g-h).

Specifically in the head, while Cre activity was observed starting at E11.5, the cleft face phenotype in *Vps25*$^{fl/fl}$*;R26R*$^{nTnG/+}$*;Shox2*$^{IRES-Cre/+}$ embryos was not detectable until

E12.5 (Supplementary Figure 4a). Lineage tracing identified two distinct populations of Cre+ cells in the murine midface at E11.5 and E12.5 (Supplementary Figure 4a-b). The first was a midline population that underwent early apoptosis. The second was located at the junction between the maxillary and mandibular prominences (Supplementary Figure 4a-b). By E12.5, this latter population had expanded (Supplementary Figure 4a-b) and now extended into the lateral palatal process (LPP)- that will form the palatal shelf. Unlike the midline population, the LPP population showed negligible cell death (Supplementary Figures 4c-d). Notably, RUNX2 was detected in a subset of GFP^+ cells within this population (Figure 4d, bottom panels). Based on these findings, we focused all further studies on the embryonic region spanning the palatal shelves (PS) and the maxillary-mandibular junction (M) -collectively referred to as the PSM domain- where the cephalic cell population of interest resides.

At E13.5, GFP signal was still detectable in the PSM of *Vps25$^{fl/fl}$;R26R$^{nTnG/+}$;Shox2$^{IRES-Cre/+}$* embryos (Figure 2i). Consistently, we observed impaired palatal shelf elevation in *Vps25$^{fl/fl}$;Shox2$^{IRES-Cre/+}$* embryos, mimicking the *Vps25$^{ENU/ENU}$* cleft phenotype (Figure 2j). Altogether, characterization of the tissue-specific roles of VPS25 demonstrates that epithelial VPS25 is critical for PS tissue growth, whereas mesenchymal VPS25 mediates PS elevation.

Mesenchymal VPS25 is essential for formation of flat and long bones.

Given the phenotypic overlap in palatal morphogenesis of *Vps25$^{fl/fl}$;Shox2$^{IRES-Cre/+}$* and *Vps25$^{ENU/ENU}$* embryos, we next explored whether formation of both intramembranous and endochondral bones was affected upon *Vps25* mesenchymal loss, similarly to *Vps25* constitutive hypomorphic loss. First, we determined whether Cre activity was observed in tissues undergoing ossification. At E15.5, GFP signal was detected in regions of the face and limbs undergoing bone formation in *R26R$^{nTnG/+}$;Shox2$^{IRES-Cre/+}$* embryos (Figure 3a). Alcian blue staining did not reveal gross alterations in cartilaginous structures of *Vps25$^{fl/fl}$;Shox2$^{IRES-Cre/+}$* mutant *versus Vps25$^{fl/+}$;Shox2$^{IRES-Cre/+}$*control embryos (Figure 3b). However, bony structures were absent in limb and craniofacial

Cre+ tissues from *Vps25*$^{fl/fl}$;*Shox2*$^{IRES\text{-}Cre/+}$ homozygous mutant embryos compared to controls (Figure 3c). Upper views of homozygous mutant and control heads confirmed the formation of cartilaginous structures despite the drastic craniofacial clefting in mutants (Figure 3d). In addition, the premaxillary bone failed to form in *Vps25*$^{fl/fl}$;*Shox2*$^{IRES\text{-}Cre/+}$ mutant embryos, as demonstrated by alizarin red-staining (Figure 3e). Abnormal bone formation was confirmed by a decreased ALPL signal (Figure 3f) and significantly lower *Alpl* transcript levels in *Vps25*$^{fl/fl}$;*Shox2*$^{IRES\text{-}Cre\ /+}$ compared to *Vps25*$^{fl/fl}$;*Shox2*$^{+\ /+}$ or *Vps25*$^{fl/+}$;*Shox2*$^{+\ /+}$ control palatal tissue (Figure 3g). Unlike in E12.0 *Vps25*$^{ENU/ENU}$ BA1 mesenchyme, reduction of *Runx2* was not significant in E14.5-E15.0 mutant *versus* control mesenchymal palatal tissue. However, increased *Plod3* (lysyl hydroxylase 3) transcript levels suggested abnormal collagen synthesis in *Vps25*$^{fl/fl}$;*Shox2*$^{IRES\text{-}Cre\ /+}$ mutant PS (Figure 3g). Overall, our findings show that mesenchymal VPS25 is required for osteogenesis in both flat intramembranous bones, including the secondary palate, and long endochondral bones, including the limbs.

Loss of mesenchymal VPS25 leads to upregulation of IGF signaling.

To dissect perturbed molecular mechanisms that could account for defective bone formation upon *Vps25*-mesenchymal deletion, we conducted bulk RNA-seq on E12.5 *Vps25*$^{+/+}$;*Shox2*$^{IRES\text{-}Cre/+}$ control and *Vps25*$^{fl/fl}$;*Shox2*$^{IRES\text{-}Cre/+}$ mutant craniofacial PSM (Figure 2a and Supplementary Figure 4b). Differentially expressed genes (DEGs) in *Vps25*$^{fl/fl}$;*Shox2*$^{IRES\text{-}Cre/+}$ mutant compared to *Vps25*$^{+/+}$;*Shox2*$^{IRES\text{-}Cre/+}$ control PSM revealed upregulation of the chondrogenic marker *Sox9*[8,68], as well as genes encoding components of the Insulin-like Growth Factor (IGF) pathway[1] (Figure 4a). Conversely, multiple genes encoding ESCRT-III components were downregulated in mutant *versus* control PSM. Pathway analysis of DEGs identified endochondral ossification as one of the most downregulated pathways in mutant *versus* control PSM (Figure 4b). Significant upregulation of *Sox9* and *Igf1r* was validated by qRT-PCR in E14.5-E15.0 mutant compared to *Cre*-negative control PS (Figure 4c). Dysregulation of additional genes previously associated with craniofacial development or phenotypes, such as *Efna1*[69],

Zfhx3[70], and genes encoding proteins containing AT-rich interaction domains (ARID)[71,72], were also perturbed in mutant *versus* control PSM at E12.5, as shown by qRT-PCR (Supplementary Figures 5a-b).

We next evaluated protein levels and activation of the main IGF receptor in cartilage and bone[1], IGF1R, in mutant *versus* control tissue. Our strategy was based on the observations that 1) components of the IGF signaling pathway are upregulated in mutant compared to control PSM, including IGF binding protein 5 (IGFBP5), which is an IGF1 downstream target in chondrocytes[73]; and 2) the ESCRT machinery regulates the turnover of activated membrane receptors[30,74]. Immunodetection of total and activated IGF1R receptor by Tyrosine 1135-1136 phosphorylation showed a significant accumulation of both forms in E12.5 $Vps25^{fl/fl};Shox2^{IRES\text{-}Cre/+}$ homozygous mutant *versus* $Vps25^{fl/+};Shox2^{IRES\text{-}Cre/+}$ control PSM (Figures 4d-e). Similarly, a significant IGF1R accumulation was observed in BA1 tissue from E11.5 $Vps25^{ENU/ENU}$ hypomorphic mutants compared to controls (Figures 4f-g). Although the increase in activated IGF1R levels did not reach statistical significance in $Vps25^{ENU/ENU}$ *versus* $Vps25^{+/+}$ BA1 by western blot quantification, its accumulation in the developing mutant palate was clearly detectable by immunofluorescence on coronal sections (Figure 4.h). Collectively, these findings reveal IGF1R accumulation as a consequence of *Vps25* developmental loss in cephalic mesenchymal tissues.

Vps25 mesenchymal loss during skeletal development results in downregulation of osteogenic markers and upregulation of chondrogenic genes.

As IGF signaling is involved in both osteo- and chondrogenesis[1], and bulk RNA-Seq analyses revealed upregulation of *Sox9*[8,68] -encoding a master chondrogenic transcription factor- upon *Vps25* mesenchymal loss, we investigated the cellular and molecular basis of chondrocyte and osteoblast differentiation in this mouse mutant model. No detectable changes in the morphology or distribution of GFP+ cells were detectable in coronal sections from mutant *versus* control PSM at E13.5, a stage of active chondrogenesis[8] (Figure 5a).

Osteoblasts and Chondrocytes derive from the same mesenchymal progenitors, which co-express the genes encoding SOX9 and RUNX2[2,4]. Relative levels of these transcription factors modulate lineage determination, by inducing expression of lineage-specific genes[2,4] (Figure 5b). To assess a potential fate shift of mesenchyme progenitors towards chondrogenic lineages in mutant tissue, we FACS-sorted GFP+ and GFP- cells from E12.5 *Vps25$^{fl/+}$;R26R$^{nTnG/+}$;Shox2$^{IRES-Cre/+}$* control and *Vps25$^{fl/fl}$;R26R$^{nTnG/+}$;Shox2$^{IRES-Cre/+}$* mutant PSM. Quantification of transcripts for specific osteogenic and chondrogenic markers by qRT-PCR confirmed increased *Sox9* expression in GFP+ and GFP- cells (Figures 5c-d), suggesting increased chondrogenesis in mutant tissue in a cell-autonomous and non-cell- autonomous manner. In addition, the mRNA for *Col2a1*, a marker of proliferating chondrocytes[8,75], was similarly upregulated in mesenchymal GFP+, *Vps25*-null cells *versus* GFP+ control cells (Figure 5c). While no significant changes in *Runx2* transcripts were detected in E12.5 mutant PSM cells, we found markedly decreased RUNX2 protein levels in E13.5 mutant PSM (Figure 5e). Specifically, GFP+ cells from E13.5 *Vps25$^{fl/+}$;R26R$^{nTnG/+}$;Shox2$^{IRES-Cre/+}$* control PSM cells were also RUNX2+, while in *Vps25$^{fl/fl}$;R26R$^{nTnG/+}$;Shox2$^{IRES-Cre/+}$* mutants these cells were, for the most part, RUNX2- (Figure 5e). Furthermore, the SOX9+ domain was expanded in *Vps25$^{fl/fl}$;R26R$^{nTnG/+}$;Shox2$^{IRES-Cre/+}$* mutant compared to *Vps25$^{fl/+}$;R26R$^{nTnG/+}$;Shox2$^{IRES-Cre/+}$* control PSM (Figure 5f). As SOX9 is critical for embryonic CNCC chondrogenic fate commitment[4,8], while RUNX2 is required for CNCC osteogenic differentiation, including the craniofacial complex[4,6,22,76], these results suggest that loss of mesenchymal *Vps25* favors chondrogenic over osteogenic fate commitment *in vivo*.

Persistent expression of chondrogenic markers upon *Vps25* loss in a model of *in vitro* osteogenic induction.

To further investigate whether cells from *Vps25* mutant PSM exhibit increased commitment to a chondrogenic *versus* an osteogenic fate, we cultured PSM primary cells for *in vitro* osteogenic induction. 20% of PSM cells obtained from control tissue

were GFP+, while a significantly lower percentage of those cells were GFP+ in mutant PSM tissue (Figure 6a). After 10 days of *in vitro* induction in osteogenic media (Figure 6b), cells isolated from E12.5 *Vps25*$^{fl/+}$;*R26R*$^{nTnG/+}$;*Shox2*$^{IRES\text{-}Cre/+}$ control PSM exhibited detectable levels of SP7, while SOX9 was negligible(Figure 6c). In contrast, SOX9 persisted in cultured cells isolated from *Vps25*$^{fl/fl}$;*R26R*$^{nTnG/+}$;*Shox2*$^{IRES\text{-}Cre/+}$ mutant PSM. Moreover, these SP7+ cells present in the mutant cultures were also SOX9+, suggesting abnormal fate commitment (Figure 6c). Western blot analyses, after 10 days of osteogenic induction, confirmed drastic downregulation of osteogenic markers SP7, ALPL, and COL1A1 with concomitant upregulation of the late chondrogenic marker COL2A1 in cells isolated from *Vps25*$^{fl/fl}$;*R26R*$^{nTnG/+}$;*Shox2*$^{IRES\text{-}Cre/+}$ mutant PSM compared to cells obtained from control tissue (Figures 6d-e). Accumulation of COL2A1 in cells from mutant PSM after osteogenic induction was confirmed by immunofluorescence (Figure 6f). Altogether, these results uncover abnormal osteogenic differentiation of cultured mesenchymal cells, accompanied by upregulation of critical chondrogenic markers, upon VPS25 loss – similar to the phenotypes observed *in vivo* in mutant embryos (Figure 5).

Pharmacological inhibition of IGF1R restores osteogenic differentiation in cells from *Vps25*-deficient murine tissue.

To determine whether aberrant expression of chondrogenic markers is dependent on IGF1R activity in cells from mutant tissues, we treated *in vitro* osteogenically induced cultures with a specific IGF1R inhibitor, PQ-401[77,78] (Figure 7a). In *Vps25*$^{+/+}$ BA1 cultured cells treated with vehicle, abundant SP7 was detectable after 20 days of osteogenic induction, while SOX9 was present only in a few cells. IGF1R inhibition led to further decrease of SOX9+ cells (Figure 7b). Conversely, in *Vps25*$^{ENU/ENU}$ BA1 cultured cells treated with vehicle, most SP7+ cells were also SOX9+. Notably, PQ-401 treatment resulted in a drastic decrease of SOX9+ cells, comparable to control conditions (Figure 7c).

Next, we assessed whether IGF1R inhibition impacted the ability of mutant cells to deposit mineralized matrix *in vitro.* We cultured cells from *Vps25*$^{fl/fl}$*;R26R*$^{nTnG/+}$*;Shox2*$^{IRES\text{-}Cre/+}$ and *Vps25*$^{ENU/ENU}$ mutant embryos, together with their respective controls, until terminal stages of osteogenic differentiation (Figures 7d and Supplementary Figure 6a). Extracellular calcium deposition was assessed by alizarin red staining. Because PQ-401 also affects cell proliferation[77,78], we normalized alizarin red to crystal violet staining as a readout for cell density. Cells isolated from both *Vps25*$^{fl/fl}$*;R26R*$^{nTnG/+}$*;Shox2*$^{IRES\text{-}Cre/+}$ and *Vps25*$^{ENU/ENU}$ tissues formed a significantly higher amount of mineralized calcium matrix when treated with PQ-401 *versus* vehicle (Figures 7e-f and Supplementary Figure 6b-c). In addition, *Runx2* expression increased in PQ-401-treated cells isolated from *Vps25*$^{fl/fl}$*;R26R*$^{nTnG/+}$*;Shox2*$^{IRES\text{-}Cre/+}$ mutant PSM after 10 days of osteogenic induction, reaching transcript levels similar to those observed in vehicle-treated control cells (Figure 7g). Our data prove that upregulation of IGF signaling is responsible, at least in part, for the impaired ossification phenotype observed in cultured cells isolated from *Vps25*-deficient tissue.

Vps25 loss triggers an abnormal chondrogenic program through IGF1R upregulation in the mouse.

IGF signaling not only promotes chondrocyte proliferation but also induces hypertrophy during endochondral ossification[79–83]. Of note, chondrocyte hypertrophy is a specialized cellular behavior observed only in endochondral bones[2], absent in most CNCC-derived facial bones[4,22]. Collagen 10 (COLX) is a known marker of hypertrophic chondrocytes[5,11]. Accordingly, we evaluated *Col10a1* transcript levels in *in vitro* osteogenically induced cells isolated from E12.5 *Vps25*$^{fl/fl}$*;R26R*$^{nTnG/+}$*;Shox2*$^{IRES\text{-}Cre/+}$ mutant and *Vps25*$^{fl/fl}$*;R26R*$^{nTnG/+}$*;Shox2*$^{+/+}$ as well as *Vps25*$^{fl/+}$*;R26R*$^{nTnG/+}$*;Shox2*$^{IRES\text{-}Cre/+}$ control PSM tissues (Figure 8a). *Col10a1* expression was significantly upregulated in vehicle-treated cells from homozygous mutant *versus* control PSM. Notably, PQ-401 treatment led to a drastic decrease of *Col10a1* transcript levels (Figure 8b).

In order to conduct similar pharmacologic inhibition assays *in vivo*, we used the tamoxifen-inducible *CAGGCre-ER^{TM}* mouse line[84] to determine the timepoint when *Vps25* loss triggers abnormal skeletal differentiation. When tamoxifen was injected into pregnant dams at 11.5 da*ys post coitum* (d.p.c.) -to inactivate *Vps25* at the onset of craniofacial chondrogenesis[8,85] (Figure 8c)- we observed decreased or absent areas of bone by RGB-trichrome staining in E14.5 homozygous mutant embryos compared to heterozygous controls (Figure 8d). *Vps25$^{fl/fl}$;CAGGCre-ER$^{TM/+}$* embryos exposed to tamoxifen at E11.5 also exhibited enlarged brain ventricles (Figure 8d), a phenotype that has been previously reported in mice and humans with *Vps25*-*VPS25* mutations[51]. Impaired elevation of palatal shelves in homozygous *Vps25$^{fl/fl}$;CAGGCre-ER$^{TM/+}$* mutants (Figure 8d) mimicked the phenotype seen in *Vps25* hypomorphic mutants and in embryos with *Vps25* loss in PSM mesenchyme (Figure 2j). Abnormal distribution of the SP7+ domain as well as increased levels of COL2A1 in upper and lower jaw were observed by immunofluorescence in E14.5 homozygous mutant embryos compared to heterozygous controls (Figure 8e). In addition, homozygous mutant embryos exhibited an increased intensity of the cartilage marker Aggrecan (ACAN) and a significantly enlarged nasal septum cartilage (NSC) area than heterozygous control head (Supplementary Figures 7a-b). Western blot analyses showed a drastic reduction not only of VPS25 but also of the other ESCRT-II subunit VPS36[86] in homozygous mutant PSM 24 hours after the first tamoxifen injection (Supplementary Figures 7c-d), consistent with prior evidence for downregulation of all ESCRT-II subunits after depletion of one component[87–89]. It is noteworthy that *Vps25* homozygous deletion at later timepoints, coinciding with the onset of craniofacial osteogenesis[90] (Supplementary Figure 7e), did not lead to abnormal embryonic ossification, despite resulting in secondary palate posterior clefting (Supplementary Figures 7f-h). These findings support an early role for VPS25 in skeletal cell commitment.

Next, to evaluate the *in vivo* roles of IGF1R in cartilage and bone formation upon *Vps25* loss, we injected pregnant dams with vehicle or the specific IGF1R inhibitor Picropodophyllin (PPP)[91,92] at 10.5, 11.5, and 12.5 d.p.c. (Figure 8f). E14.5 mutant *Vps25$^{ENU/ENU}$* heads exposed to PPP exhibited thinner or even absent cartilaginous structures compared to vehicle treated *Vps25$^{ENU/ENU}$* heads. (Figure 8g). At E15.5, bony

structures were larger in heads from mutant embryos treated with PPP *versus* vehicle (Figure 8h). PPP treatment did not impact osteogenesis in heads from wildtype embryos. Collectively, our findings establish that VPS25 loss promotes a hypertrophic-like phenotype *in vitro* and enhances chondrogenesis at the expense of bone formation during early murine skeletal development, at least partially via IGF1R upregulation.

Aberrant IGF1R endo-lysosomal trafficking in VPS25-deficient cells is rescued by pharmacological inhibition of the pathway.

In multiple biological contexts, LOF of ESCRT-encoding genes results in sustained activation of membrane receptors by their trapping in endosomal compartments[46,50,93]. To evaluate intracellular accumulation of IGF1R upon VPS25 loss, we conducted LAMP1 and IGF1R immunofluorescence in osteogenically induced *Vps25*$^{+/+}$ and *Vps25*$^{ENU/ENU}$ murine BA1 cells cultured for 10 days. We observed that IGF1R remains trapped in intracellular LAMP1+ late endosomes/lysosomes[94] in cells from *Vps25*$^{ENU/ENU}$ embryos. Strikingly, pharmacological inhibition of IGF1R transphosphorylation at the plasma membrane prevented its intracellular accumulation in mutant cells, while its localization remained unaffected in *Vps25*$^{+/+}$ cells. (Figure 9a-b).

To determine whether ESCRT-dependent regulation of IGF1R is conserved in humans, we measured activated IGF1R levels in primary fibroblasts from healthy control individuals and from patients carrying biallelic *VPS25* variants[51]. We performed western blot analyses to quantify degradation of the activated receptor after IGF1 pulse(Figure 9c). Compared to control cells, patient cells showed higher IGF1R activation immediately after IGF1 exposure, and this activation remained significantly elevated for up to two hours (Figure 9d). In parallel, we assessed IGF1R subcellular localization immediately after IGF1 pulse and two hours after IGF1 exposure by immunofluorescence. Because IGF1R is also subjected to proteasomal degradation upon ligand-mediated activation[95], cells were treated with the proteosome inhibitor MG-132 to evaluate only endosomal contribution to IGF1R stability. We observed IGF1R localization to late endosomes/lysosomes immediately after IGF1 pulse in control and

mutant cells. Similar to our findings in *Vps25*-deficient mouse cells, IGF1R remains trapped in enlarged LAMP1+ compartments in cells from patients *versus* controls. IGF1R accumulation in engorged LAMP1+ vesicles persists up to two hours after IGF1 exposure (Figure 9e). Together with the overlapping craniofacial phenotypes of *Vps25*-deficient mouse models and patients with recessive *VPS25* mutations[46,51,52], these findings support an evolutionarily conserved role for VPS25/ESCRT-II in mediating IGF1R degradation in mammals.

DISCUSSION

Bones are shaped through endochondral ossification, which requires a cartilage template to mold the bone[3,5,22,29], or intramembranous ossification, where bones develop from condensations that directly undergo osteoblast differentiation[2,3]. Most craniofacial bones -including palatal shelves[96]- are formed by intramembranous ossification[4,22], which still remains poorly understood[2,29]. Here, we have uncovered a new role for the ESCRT-II encoding gene *Vps25* in regulating balanced cell lineage commitment during skeletal differentiation. Mechanistically, we identified IGF1R as a yet-unrecognized receptor regulated by the ESCRT machinery in mice and humans. In particular, we described that abnormal accumulation and ensuing hyperactivation of IGF1R lead to impaired osteogenic commitment.

During endosomal maturation, ligand-receptor complexes are sorted into early endosomes for degradation in the endo-lysosomal pathway[97]. Receptors are monoubiquitylated upon activation, allowing the recruitment of ESCRT subunits to the endosomal membrane through their ubiquitin binding domains[33,97]. The endosomal membrane is then bent and severed in an ESCRT-dependent manner, forming intraluminal vesicles (ILVs) within the endosomal lumen that contain endocytosed ligand-receptor complexes[32,98]. Once filled with ILVs, the late endosome fuses with lysosomes for cargo degradation[32,98], thus attenuating signaling pathways[30,97], some of them key for skeletal development[99,100]. Similar to other ESCRT-regulated receptors[101,102], IGF1R ubiquitylation upon ligand binding is necessary for its

internalization and lysosomal degradation in cells[95,103–105]. However, until now, a direct link between IGF1R trafficking and the ESCRT machinery had not been established.

Our results show that loss of the ESCRT-II subunit VPS25 leads to increased cartilage formation at the expense of osteogenesis in the mouse embryo and skews skeletal commitment towards a chondrogenic fate in murine cultured cells. This mutant skeletal phenotype is mediated -at least partially- by hyperactivation of IGF signaling, as demonstrated by pharmacological rescue experiments *in vitro* and *in vivo*. The partial rescue of the *Vps25* mutant skeletal phenotype upon IGF1R inhibition may reflect inefficient delivery of the compound to the developing embryos or a suboptimal pharmacological regimen. Lastly, concomitant contributions of other ESCRT-regulated signaling molecules relevant to craniofacial morphogenesis -such as the NOTCH pathway[41,52,106,107]- cannot be ruled out. Nonetheless, these novel findings highlight the potential of pharmacologically targeting signaling pathways to prevent or rescue craniofacial abnormalities *in utero*.

IGF signaling participates in multiple aspects of skeletal development, growth, and repair[1,80,108]. For instance, mouse models with osteoblast-specific attenuation of IGF1 signaling exhibit reduced mineral deposition[109–111]. In addition, chondrocyte-specific inactivation of IGF1 signaling leads to decline of trabecular bone mass and growth retardation of long bones likely due to reduced hypertrophy[80,83,109,112]. Although these data differ from the results presented here, they reflect later roles of IGF1 signaling. Indeed, the *Cre* lines used in the above studies were active in bone and cartilage only after osteochondroprogenitor commitment[110,111,113]. Collectively, these findings demonstrate distinct, stage-specific functions for IGF1 signaling during bone and cartilage development.

Dysregulation of IGF signaling in humans has been linked not only to skeletal conditions such as osteoarthritis[114], condylar hyperplasia[115], and heterotopic ossification[116], but also to craniofacial defects[117–119]. Similarly, in addition to neonatal encephalopathy, patients with mutations in *VPS25* exhibit microcephaly and retrognathia[51], mimicking the craniofacial phenotype observed in *Vps25*-deficient mouse

embryos. It is noteworthy that in zebrafish depletion of the ESCRT-II component Vps22 (encoded by the *snf8* gene) resulted in cortical and cerebellar atrophy with stunted appearance of the head[89]. Together, our findings in mice and in human cells establish a conserved ESCRT-dependent regulation of IGF1R in mammals.

IGF1R trapping and accumulation in intracellular LAMP1+ compartments of VPS25 deficient cells can lead to its “internalized activation”, which results in activation of select downstream signaling effectors upon intracellular internalization[120,121]. Of note, it has been shown that IGF1R endocytosis and trafficking to specific intracellular compartments triggers select cellular responses, such as cell migration when IGF1R localize to the Golgi[101]. An example of the critical role for the ESCRT machinery in internalized receptor activation is provided by the trapping of the glucagon receptor (GCGR) in endosomes, where it drives sustained and specific overactivation of gluconeogenic pathways upon VPS37A/ESCRT-I loss[93].

Based on our results, we propose a model in which VPS25/ESCRT-II promotes IGF1R lysosomal degradation in CNCC-derived skeletal progenitors, which allows for balanced osteochondroprogenitor commitment. In contrast, VPS25 deficiency leads to aberrant endosomal maturation/lysosomal degradation, causing endosomal trapping with ensuing IGF1R sustained activation in cells from mice and human patients. IGF1R hyperactivation skews skeletal progenitors towards chondrogenic commitment at the expense of osteogenesis (Figure 10). The aberrant cellular behaviors observed in *Vps25* mutant cells are further spread in a non-cell autonomous manner in the surrounding mesenchymal tissue through mechanisms yet to be elucidated.

At a transcriptional level, a potential VPS25 downstream osteogenic regulator is the transcription factor MEIS2[122]. It was reported that MEIS2 represses osteogenesis in CNCC-derived mesenchyme[122]. Accordingly, CNCC-specific loss of MEIS2 caused abnormal and premature ossification in mice via upregulation of IGF2[123]. Our bulk RNA-seq datasets revealed elevated *Meis2* transcript levels in *Vps25*-deficient PSM. Whether MEIS2 similarly suppresses IGF2 in *Vps25*-mutant PSM, thereby shifting the IGF1:IGF2 balance and altering IGF receptor signaling, remains to be determined.

Notably, Zhang et al reported that ESCRT-III subunit CHMP5 -unlike VPS25/ESCRT-II- restricts endochondral bone formation[54]. These opposite roles in osteogenesis can be explained by the modular assembly of the ESCRT machinery with context-dependent functions. The five oligomeric ESCRT complexes are required for a number of cellular processes such as endosomal sorting, autophagy, lysosomal and nuclear repair, and neuron pruning[33,36]. In particular, ESCRT-II recruits ESCRT-III components[33,124] for their polymerization on cellular membranes and subsequent scission by the VPS4 ATPase[33,36]. It has been reported that in mammals, ESCRT-III subunits exhibit differential binding affinity and/or stability to other ESCRT components and membranes[33,125,126]. ESCRT-III subunits can bind in different stoichiometry to membranes with various degrees of curvatures, displaying diverse assembly dynamics and functions[125,127]. For example, CHMP7 is involved in maintenance of inner nuclear membrane morphology[128]; CHMP4C in inheritance of the midbody remnant for primary cilium assembly in kidney cells[129]; and CHMP5 in initiating and maintaining T-cell acute lymphoblastic leukemia[130]. Our data show that loss of mesenchymal VPS25 leads to not only a drastic reduction of the ESCRT-II subunit VPS36 -consistent with previous reports after depletion of single ECRT-II subunits[87–89]- but also to a significant decrease of ESCRT-III encoding gene transcripts *Chmp2b*, *Chmp6*, and *Chmp3*. Hence, it is not surprising that deletion of *Vps25 versus* other ESCRT-encoding genes can result in different and even opposite skeletal phenotypes. Together, these findings underscore that in mammals distinct cellular processes depend on particular ESCRT subunit combinations, rather than ESCRT subunits interchangeably. These organismal-level insights were made possible only by working with complex animal models, which capture tissue and organ physiology that simpler systems cannot.

Overall, this study uncovered IGF1R as a yet-unrecognized ESCRT-dependent driver of skeletal lineage commitment/differentiation in mammals, opening new avenues to expand the scarce toolkit of chondro- and osteo-inductive molecules. Ultimately, our results can be harnessed towards the design of unexplored strategies for future treatment, reconstruction, and regeneration of skeletal structures, including those of the human craniofacial complex.

METHODS

Animal Models

All animal protocols were approved and conducted in accordance with institutional guidelines for animal care by the University of California, San Francisco Institutional Animal Care and Use Committee (IACUC). Mice were grouped-housed at the University of California, San Francisco Laboratory Animal Resource Center (LARC), a temperature-controlled pathogen-free facility, with 12 h light:dark cycles and ad-libitum access to food and water. *Vps25*^{ENU} animals carrying a hypomorphic allele with a G-to-A transition in intron 3 of the *Vps25* gene were generated by N-ethyl-N-nitrosourea (ENU) mutagenesis[131], described elsewhere[46]. *Vps25*^{flox} allele was generated by the University of Michigan Transgenic Animal Model Core using EasiCRISPR[61,62] to introduce exon2-flanking loxP sites. Briefly, sgRNAs 5'-CAGCCTAGCAGCACGTTAGG-3' and 5'-TGCCTACTGTGGGTAAAGGG-3' (Synthego), the Cas9 protein (SigmaAldrich), and the single stranded DNA donor (IDT, coordinates chr11:101253868-101254375) were microinjected into zygotes from B6SJLF1 mice (Jackson Laboratory stock no. 100012). G0 founders confirmed by PCR and Sanger sequencing were mated to wildtype C57BL/6J (Jackson Laboratory stock no. 000664) animals for 11 generations. Constitutive early embryonic deletion was assessed by qPCR using a β-actin *Cre* deleter line[132] (Jackson Laboratory stock no. 033984). *Vps25*^{flox} animals were mated to *Wnt1-Cre*^{Tg} (Jackson Laboratory stock no. 022137)[65], *Crect*^{Cre}[63], tamoxifen-inducible *CAGGCre-ER*^{TM} (Jackson Laboratory stock no. 004682)[84], or *Shox2*$^{IRES\text{-}Cre}$ carriers[67]. The reporter line *R26R*^{nTnG} (Jackson Laboratory stock no. 023537)[66] was used for lineage tracing. All experiments were conducted using two *Vps25*^{flox} clones. For timed *Vps25* embryonic deletion, pregnant mice were injected with tamoxifen:progesterone in a 2:1 ratio in corn oil for two consecutive days. 0.03 mg of tamoxifen were injected at 11.5 days post coitum (d.p.c.), while 0.04 mg were injected at 12.5 and 13.5 d.p.c. Picropodophyllin (PPP, HY-15494 MedChemExpress) was dissolved in 5% DMSO-95% corn oil at a final concentration of 2.5 mg/mL. Pregnant dams were injected at 10.5,11.5, and 12.5 d.p.c. with 10 mg/Kg of PPP or with an equivalent volume of 5% DMSO-95% corn oil as vehicle control.

Pregnant females were euthanized by CO_2 inhalation followed by cervical dislocation for embryo retrieval. Genotyping was conducted by PCR from tail biopsies or yolk sac tissue, using the genotyping primers listed in Supplementary Table 1.

Cell culture

All cells were cultured at 37 °C and 5% CO_2. Branchial arch 1 (BA1) or PSM were collected from individual embryos at gestational day (E) 11.5 and 12.5, respectively. Dissected tissue was rinsed with cold Phosphate Saline Buffer (PBS, Gibco) and digested with 0.25% Trypsin-EDTA (HyClone) for 5 minutes at 37 °C. Trypsin was inactivated with Dulbecco's Modified Eagle Medium (DMEM, Corning) supplemented with 20% Fetal Bovine Serum (FBS, Gibco). After resuspension, cells were filtered using 40 µm cell strainers. Cells were centrifuged and seeded in Mesenchymal Stem Cell Media (Promocell) supplemented with 100 U/mL of Penicillin-Streptomycin (HyClone). Osteogenic differentiation media (MesenCult™ Mouse Osteogenic Stimulatory Kit, StemCell Technologies) supplemented with Penicillin-Streptomycin and L-glutamine 2 mM was added to >90% confluent cultures. PQ-401 at 10 µM (HY-13686, MedChemExpress) or DMSO (vehicle) were added on the fifth day of osteogenic induction and replaced every two days.

Human primary fibroblasts, provided by Dr. Lama AlAbdi from King Faisal Hospital and Research Centre (Saudi Arabia), were derived from skin biopsies of patients with recessive *VPS25* variants or from healthy donors, following IRB-approved research protocols. All skin biopsies were obtained from male patients and healthy donors aged 21-36 months, with the exception of one 8 year-old female patient. *VPS25* mutations identified by exome sequencing showed a homozygous c.22C>T (p.Pro8Ser) variant in two of the patients and a c.23C>T; c.514G>A (p.Pro8Leu;p.Gly172Ser) compound mutation in the 8-year-old female patient. All patients presented with a lethal neonatal-onset encephalopathy, characterized by severe hypotonia, epilepsy, as well as brain and craniofacial anomalies, as described in a previously reported cohort[51]. Samples were de-identified prior to material transfer from the King Faisal Research Centre to the University of California, San Francisco. Primary fibroblasts were cultured in Minimum

Essential Medium Alpha (α-MEM, Gibco) supplemented with 20% FBS (One Shot Premium™, Gibco) and 100 U/mL of Penicillin-Streptomycin (Hyclone). For IGF-1 pulse, cells were serum-deprived for 20 hours followed by a 10 minute-incubation with 50 ng/mL human recombinant IGF-1 (HZ-1322 Proteintech) in serum-free α-MEM media. After IGF-1 pulse, cells were rinsed in PBS and cultured in serum-free α-MEM media. For IGF1R immunofluorescence, human fibroblasts were treated with IGF1 together with 20 μM of MG-132 (HY-13259, MedChemExpress). After IGF1 removal, cells were maintained in serum-free α-MEM medium containing 20 μM MG-132 for 2 hours.

Alizarin red and crystal violet staining in cultured cells

After *in vitro* osteogenic differentiation in 96-well plates, cells were fixed in 4% paraformaldehyde (PFA) and stained for 45 minutes in 2% alizarin red in water pH 4.2 at room temperature on a rocking platform in the dark. Alizarin red was extracted as described by Benar et al[133]. Briefly, cells were rinsed with water and 50 μL of 10% acetic acid was added to each well. Cells were mechanically detached and transferred to a tube for incubation at 85 °C and 750 rpm agitation. Samples were then transferred to ice for 5 minutes and centrifuged at 17,000 xg for 10 minutes at 4 °C. Once the supernatants were transferred to a new 96-well plate, 13 μL of 10% ammonium hydroxide was added to each well. Calcium-bound alizarin red absorbance was measured at 405 nm.

Crystal violet measurements carried out according to Feoktistova et al[134], by staining cells with a 0.5% crystal violet staining solution in water for 20 minutes at room temperature on a rocking platform. After rinsing with tap water, crystal violet was extracted with methanol for 20 minutes at room temperature with gentle rotation. Crystal violet absorbance was measured at 570 nm. All measurements were obtained using GloMax Explorer microplate reader (Promega).

Whole mount alizarin red staining

E15.5 embryos were collected form pregnant females and fixed in PFA at 4 °C overnight. Embryos were then rinsed in water and stained in a 0.004% alizarin red and

0.5% KOH solution overnight with rotation at room temperature. Embryos were cleared in 0.5% KOH and 20% Glycerol overnight at room temperature in rotation and stored in Glycerol:Ethanol:Benzyl alcohol 2:2:1 until imaging with a M205FA stereomicroscope (Leica).

Whole mount alcian blue staining

Following the protocol described by Nagy et al[135], E14.5 embryos were dissected and fixed in Bouin's solution for five hours at room temperature in rotation. Embryos were rinsed in a 70% ethanol and 0.1% NH_4OH solution until they looked pale. After equilibration in 5% acetic acid, cartilage was stained with 0.05% alcian blue in 5% acetic acid for five hours at room temperature in rotation. Embryos were rinsed twice in 5% acetic acid for 1 hour and dehydrated in methanol twice for 1 hour followed by clearing in BABB and imaging with a M205FA stereomicroscope (Leica).

RGB trichrome staining

Embryonic heads were fixed in 4% PFA, dehydrated in alcohol series, and cleared with Histoclear-II for paraffin embedding. 10 µm were obtained with a RM2245 microtome (Leica). After paraffin removal with Histoclear-II and rehydration in alcohol series, sections were stained at room temperature as described by Gaytan et al[55], with 1% alcian blue in a 3% acetic acid solution pH 2.5 for 20 minutes, followed by tap water rinsing and staining with 0.04% fast green for 20 minutes. After rinsing with tap water, sections were stained with 0.1% sirius red in saturated aqueous solution of picric acid for 30 minutes and rinsed in two changes of 1% acetic acid in tap water. Finally, sections were dehydrated in alcohol series, cleared in Histoclear-II, and mounted with Omnimount (National Diagnostics) for imaging using a CX43 upright microscope with an LC35 camera (Olympus).

Immunohistochemistry

10 µm sections from PFA-fixed, paraffin-embedded embryonic heads were cleared with Histoclear-II and rehydrated in alcohol series. Immunohistochemistry was performed using the rabbit specific HRP/DAB Detection IHC Detection Kit with Micropolymer

(ab236469, Abcam), following the manufacturer's instructions. SP7 was detected with anti-SP7 antibody (ab22552 Abcam, 1:150) after antigen retrieval in a pH 6.0 solution with sodium citrate 10mM and 0.05% Tween 20, boiling in microwave for three minutes. VPS25 and alkaline phosphatase were detected using anti-VPS25 (A13132 Abclonal, 1:200,) and anti-ALPL (11187-1-AP Proteintech, 1:200) antibodies, respectively, after antigen retrieval in a pH 9.0 solution with Tris 10mM, EDTA 1mM, and 0.05% Tween 20, in a pressure cooker for three minutes. Primary antibodies were incubated overnight in humid chamber at 4 °C. After immunodetection, sections were counterstained with hematoxylin, dehydrated, and cleared with Histoclear-II for mounting with Omnimount media (National Diagnostics). Sections were imaged using a CX43 upright microscope with an LC35 camera (Olympus).

Immunofluorescence

Murine embryonic tissue was fixed in 4% PFA overnight at 4 °C, subjected to sucrose gradient, and embedded in OCT. 12 µm sections were obtained in Cryostar NX70 Cryostat (Thermo Scientific). Primary cells were seeded on coverslips previously coated with 1 µg/cm^2 of human fibronectin (Corning). Once treated, cells were fixed in 4% PFA for 15 minutes at room temperature. Immunofluorescence on murine tissue and cells was conducted after permeabilization with 0.5% Triton in PBS for 15 minutes, using the M.O.M. (Mouse on Mouse) Immunodetection Kit (BMK-2202 Vector Laboratories) according to the manufacturer's instructions. Primary antibodies were incubated overnight in humid chamber at 4 °C. On the following day, sections and cell-containing coverslips were incubated with M.O.M. Biotinylated anti-mouse IgG reagent for 30 minutes at room temperature in humid chamber, followed by one-hour incubation with 1:200 DyLight 549-conjugated Streptavidin (SA-5549 Vector Laboratories), 1:200 secondary antibodies conjugated to Alexa Fluor 488 or 647 (Invitrogen), and 1:500 DAPI or Phalloidin-iFluor 405 (ab1766752 Abcam, 1:500).

The following primary antibodies were used for this study: anti-VPS25 (A13132 Abclonal, 1:400), anti-RUNX2 D1L7F (12556S Cell Signaling, 1:200), anti-SP7 764704 (MAB75471 R&D Systems, 5 µg/mL), anti-EpCAM (G8.8 Hybridoma Bank, 1:100), anti-

IGF-1Rβ F-1 (SC-390130 Santa Cruz Biotechnology, 1:200), anti-phospho IGF-1Rβ 19H7 Tyr1135/36 (3024S Cell Signaling, 1:150), anti-SOX9 (AB5535 Millipore, 1:1000), anti-Aggrecan (13880-I-AP Proteintech, 1:150), anti-COL2A1 (Proteintech 28459-I-AP 1:150), anti-LAMP1 (1D4B Hybridoma Bank, 1:250), anti-GFP (GFP-1010 AvesLab, 1:400), anti-phospho-histone H3 Ser10 (06-570 Millipore, 1:500), anti-cleaved Caspase 3 (G748A Promega, 1:300), anti-SOX10 A-2 (SC-365692 Santa Cruz Biotechnology, 1:100), and anti-γH2AX Ser139 (14-9865-80 Invitrogen, 1:200).
Following permeabilization with 0.4% Triton in PBS for 10 minutes, human primary fibroblasts were blocked with 10% heat-inactivated FBS in PBS for one hour in humid chamber. Primary antibodies anti-LAMP1 lumenal domain (AF4800 R&D Systems, 6.65 µg/mL) and IGF1R (AF-305-NA R&D Systems, 5 µg/mL) were diluted in 1% BSA in PBS and incubated overnight at 4° C in humid chamber. The next day, cells were incubated with secondary antibodies conjugated to Alexa Fluor 488 and 568 (Invitrogen, 1:200) for one hour at room temperature.

All samples were mounted with ProLong Gold mounting media (Cell Signaling). Cells were imaged with LSM 900 Airscan confocal microscope (Zeiss). Sections were imaged with Eclipse Ti2 epifluorescence microscope (Nikon).

TUNEL staining

After incubation with secondary antibodies and DAPI, sections were treated with one volume of Enzyme solution and nine volumes of Labeling solution from the *In Situ* Cell Death Detection Kit, TMR red (12156792910 Roche) for one hour in humid chamber at room temperature in the dark. After rinsing three times with PBS, sections were mounted for imaging as described above.

Immunoblot

Samples were resuspended in lysis buffer (Tris-HCl 50 mM pH 7.4, NaCl 200 mM, $MgCl_2$ 2.5 mM, 1% Triton X-100, 0.2% Digitonin, EDTA 1 mM, 10% Glycerol) supplemented with protease and phosphatase inhibitors (Sigma-Aldrich) and sonicated with three cycles at high intensity for 30 seconds with Bioruptor UCD-200 (Diagenode).

Total protein concentration was quantified with BCA (Thermo Scientific). Samples were prepared for western blot using NuPage loading buffer (Invitrogen) supplemented with β-mercaptoethanol at 1.42 M and boiled for 5 minutes. Samples were then loaded into 4–12% gradient Bis-Tris precast protein gels (Invitrogen) for western blot. Proteins were transferred onto a PVDF membrane (Millipore-Sigma) overnight at 30 V and 4 °C. Membranes were blocked with 5% nonfat milk in TBST-T (Tris 10 mM, NaCl 150 mM, 0.05% Tween-20) for one hour at room temperature with rotation, and subsequently incubated O/N at 4 °C with the following primary antibodies diluted in TBST-T: anti-VPS25 (15669-1-AP Proteintech, 1:1000), anti-VPS36 (ab101379 Abcam, 1:2000), anti-phospho-IGF1Rβ 19H7 Tyr1135/1136 (3024T Cell Signaling, 1:1000), anti-IGF1Rβ D23H3 (9750T Cell Signaling, 1:1000), anti-SP7 764704 (MAB7547 R&D Systems, 1 µg/mL), anti-ALPL (11187-I-AP Proteintech, 1:1000), anti-COL1A1 (67288-I-Ig Proteintech, 1:1000), anti COL2A1 (Proteintech 28459-I-AP 1:1000), and anti-β Actin (20536-1-AP Proteintech, 1:5000). Membranes were rinsed in TBST-T and incubated with HRP-conjugated goat anti-mouse IgG (SA00001-1 Proteintech, 1:5000) or HRP-conjugated goat anti-rabbit IgG (SA00001-2 Proteintech, 1:5000) in 5% nonfat milk in TBST-T for one hour at room temperature. Chemiluminescent signal was detected with Supersignal West Dura ECL substrate (ThermoFisher Scientific) using the iBright 1500 imager (Invitrogen).

Fluorescence-Activated Cell Sorting (FACS)

E12.5 PSM tissues from *Vps25^{fl};R26R^{nTnG};Shox2$^{IRES\text{-}Cre}$* individual embryos were collected in Hanks' Balanced Salt Solution (HBSS, Gibco). Dissociation was conducted in HBSS with 0.5 mg/mL of Collagenase IV, 0.25 mg/mL of Collagenase D, 0.45 mg/mL of Liberase, and 0.5 mg/mL of DNAse I. Tissues were incubated in dissociation buffer at 37 °C with 350 rpm rotation for 10 minutes or until dissociation. Cells were centrifuged at 100 xg for 5 minutes at 4 °C and rinsed twice in FACS buffer (PBS, 5% FBS, EDTA 5 mM). After resuspension in FACS buffer, cells were sorted with FACS Aria (BD Biosciences) coupled to FACSDiva software (BD Biosciences) using 488 and 561 nm lasers and collected in RNA protection buffer for subsequent RNA isolation. Viability was

assessed with DAPI using the 405 laser. Quantification analyses were conducted using FlowJo software (Waters Biosciences).

RNA isolation and q-RT-PCR

RNA from FACS-sorted and cultured cells was purified with Monarch Total RNA Miniprep kit (T2010 New England Biolabs). Cells were collected in DNA/RNA Protection reagent and stored at -80 °C until RNA isolation, following the manufacturer's recommendations.

Tissues were collected in RLT Plus buffer from RNeasy Plus Micro Kit (74034, Qiagen) and stored at -80 °C until RNA isolation, following the manufacturer's recommendations. For mechanical separation of BA1 epithelium and mesenchyme, dissected BA1 tissue was incubated with 50 µL of Dispase 1mg/mL (P5317 Abnova) at 37 °C in 5% CO_2 for 20 minutes. The reaction was stopped with 50 µL of 1% BSA in PBS for 5 minutes on ice. The tissue was then placed in PBS and the epithelium was peeled off using 0.125 mm tungsten needle (Roboz). The separated epithelium and mesenchyme were centrifuged at 500 xg for 10 minutes at 4 °C. PBS was removed, the tissue was resuspended in RLT Plus buffer, and stored at -80 °C until RNA isolation. RNA concentration was measured with Qubit RNA High Sensitivity (HS) Assay Kit (Q32852 Invitrogen) in Qubit 3.0 Fluorometer (Life Technologies). cDNA was generated using the SuperScript III First-Strand Synthesis SuperMix kit (1172025 Invitrogen) according to the manufacturer's instructions, using equivalent RNA concentrations among samples. qPCR was performed using 5 µL of PowerUp SYBR Green Master Mix (Applied Biosystems) in 10 µL of reaction containing cDNA and the respective primers at 1 µM concentration. Reactions were prepared in 384 well MicroAmp Optical Reaction Plates (Applied Biosystems) and analyzed with QuantStudio 6 Flex (Applied Biosystems). The sequence of primers used for qPCR in this study are summarized in Supplementary Table 2.

Bulk RNA-seq

E12.5 PSM tissues were collected from four *Vps25*$^{+/+}$;*Shox2*$^{IRES\text{-}Cre/+}$ control and four

Vps25$^{fl/fl}$;*Shox2*$^{IRES\text{-}Cre/+}$ mutant embryos. RNA was extracted from samples as described above. RNA quality and concentration were assessed with RNA 6000 Pico Total RNA (5067–1513 Agilent) in Agilent 2100 bioanalyzer from the UCSF Parnassus Center for Advanced Technologies (PCAT). All RNA samples used for library preparation had a RIN>9. Libraries were prepared with QuantSeq 3' FWD mRNA-Seq V2 Library Prep Kit with UDI set B1 (192.24 Lexogen) following the manufacture's recommendations. Library size, concentration, and quality was assessed with the High Sensitivity DNA Kit (5067–4626 Agilent) in bioanalyzer. Libraries were normalized to 7.5 nM, pooled, and sequenced in an Illumina NovaSeq X to generate 100 base pair single-end reads. Sequencing was performed at the UCSF Center for Advanced Technology (CAT).

Bioinformatic analyses to calculate normalized counts and differential gene expression were conducted by analyzing fastq datasets in Galaxy[136] using the following packages: FastQC and MultiQC for quality control, Trimmomatic for trimming, RNA STAR to map the reads to the mouse GRCm38 (mm10) assembly, featureCounts to count the number of reads per gene mapped to the reference genome, DESeq2 to calculate differential gene expression across conditions, and Volcano Plot to generate plots for visualization. Pathway Gene Set Enrichment Analysis (GSEA) was conducted in WebGestalt[137], using the top 600 dysregulated genes in mutant versus control PSM, with a minimum of seven analytes per category for Wikipathways.

Bulk RNAseq datasets were deposited in the NCBI GEO database (accession number: GSE351768).

Quantification and statistical analysis

The number of apoptotic or proliferating cells in immunofluorescent images were manually identified, quantified, and analyzed using MATLAB (R2024B).

Western blot quantifications were performed using Fiji software[138]. Statistical analyses

and data representations were performed using Prism (GraphPad, La Jolla, CA). Data are presented as mean ± standard deviation (SD) as specified in figure legends. Statistical tests and post tests are specified for each analyses in figure legends depending on the number of conditions and comparisons (unpaired t-test for comparison between two conditions, one or two way ANOVA for multiple comparisons, with Tukey's or Šídák post-hoc tests). All experiments were conducted in at least three biological replicates, with each graph depicting the value of individual measurements.

REFERENCES

1. Ruan, X. *et al.* IGF signaling pathway in bone and cartilage development, homeostasis, and disease. *FASEB J. Off. Publ. Fed. Am. Soc. Exp. Biol.* **38**, e70031 (2024).

2. Galea, G. L., Zein, M. R., Allen, S. & Francis-West, P. Making and shaping endochondral and intramembranous bones. *Dev. Dyn. Off. Publ. Am. Assoc. Anat.* **250**, 414–449 (2021).

3. López, J. M. Bone Development and Growth. *Int. J. Mol. Sci.* **25**, 6767 (2024).

4. Dash, S. & Trainor, P. A. The development, patterning and evolution of neural crest cell differentiation into cartilage and bone. *Bone* **137**, 115409 (2020).

5. Hata, K., Takahata, Y., Murakami, T. & Nishimura, R. Transcriptional Network Controlling Endochondral Ossification. *J. Bone Metab.* **24**, 75–82 (2017).

6. Shirai, Y. *et al.* Runx2 function in cells of neural crest origin during intramembranous ossification. *Biochem. Biophys. Res. Commun.* **509**, 1028–1033 (2019).

7. Zhou, G. *et al.* Dominance of SOX9 function over RUNX2 during skeletogenesis. *Proc. Natl. Acad. Sci. U. S. A.* **103**, 19004–19009 (2006).

8. Mori-Akiyama, Y., Akiyama, H., Rowitch, D. H. & de Crombrugghe, B. Sox9 is required for determination of the chondrogenic cell lineage in the cranial neural crest. *Proc. Natl. Acad. Sci. U. S. A.* **100**, 9360–9365 (2003).

9. Lefebvre, V., Angelozzi, M. & Haseeb, A. SOX9 in cartilage development and disease. *Curr. Opin. Cell Biol.* **61**, 39–47 (2019).

10. Nakashima, K. *et al.* The novel zinc finger-containing transcription factor osterix is required for osteoblast differentiation and bone formation. *Cell* **108**, 17–29 (2002).

11. Yang, L., Tsang, K. Y., Tang, H. C., Chan, D. & Cheah, K. S. E. Hypertrophic chondrocytes can become osteoblasts and osteocytes in endochondral bone formation. *Proc. Natl. Acad. Sci. U. S. A.* **111**, 12097–12102 (2014).

12. Amarasekara, D. S., Kim, S. & Rho, J. Regulation of Osteoblast Differentiation by Cytokine Networks. *Int. J. Mol. Sci.* **22**, 2851 (2021).

13. Kornak, U. & Mundlos, S. Genetic Disorders of the Skeleton: A Developmental Approach. *Am. J. Hum. Genet.* **73**, 447–474 (2003).

14. Mundlos, S. *et al.* Mutations involving the transcription factor CBFA1 cause cleidocranial dysplasia. *Cell* **89**, 773–779 (1997).

15. Varadarajan, S. *et al.* Genetic Mutations Associated with Pierre Robin Syndrome/Sequence: A Systematic Review. *Mol. Syndromol.* **12**, 69–86 (2021).

16. Lui, J. C. *et al.* A neomorphic variant in SP7 alters sequence specificity and causes a high-turnover bone disorder. *Nat. Commun.* **13**, 700 (2022).

17. Marini, F., Giusti, F., Iantomasi, T. & Brandi, M. L. Congenital Metabolic Bone Disorders as a Cause of Bone Fragility. *Int. J. Mol. Sci.* **22**, 10281 (2021).

18. Charoenngam, N., Nasr, A., Shirvani, A. & Holick, M. F. Hereditary Metabolic Bone Diseases: A Review of Pathogenesis, Diagnosis and Management. *Genes* **13**, 1880 (2022).

19. Ettaki, I. *et al.* Missense variants weakening a SOX9 phosphodegron linked to odontogenesis defects, scoliosis, and other skeletal features. *HGG Adv.* **6**, 100404 (2025).

20. Amiri, M. A., Lavaee, F. & Danesteh, H. Use of stem cells in bone regeneration in cleft palate patients: review and recommendations. *J. Korean Assoc. Oral Maxillofac. Surg.* **48**, 71–78 (2022).

21. Tavares, A. L. P. & Moody, S. A. Advances in Understanding the Pathogenesis of Craniofacial Birth Defects. *J. Dev. Biol.* **10**, 27 (2022).

22. Kruijt Spanjer, E. C., Bittermann, G. K. P., van Hooijdonk, I. E. M., Rosenberg, A. J. W. P. & Gawlitta, D. Taking the endochondral route to craniomaxillofacial bone regeneration: A logical approach? *J. Cranio-Maxillo-fac. Surg. Off. Publ. Eur. Assoc. Cranio-Maxillo-fac. Surg.* **45**, 1099–1106 (2017).

23. National Institute of Dental and Craniofacial Research (NIDCR). Prevalence of Cleft Lip & Cleft Palate | NIDCR. https://www.nidcr.nih.gov/research/data-statistics/craniofacial-birth-defects/prevalence.

24. GBD 2019 Fracture Collaborators. Global, regional, and national burden of bone fractures in 204 countries and territories, 1990–2019: a systematic analysis from the Global Burden of Disease Study 2019. *Lancet Healthy Longev.* **2**, e580–e592 (2021).

25. Tabrizi, R., Shafiei, S., Moslemi, H., Dastgir, R. & Peacock, Z. S. Impact of Osteoporosis on Autogenous Bone Graft Resorption. *J. Oral Maxillofac. Surg. Off. J. Am. Assoc. Oral Maxillofac. Surg.* **82**, 961–967 (2024).

26. Hurley, C. M. *et al.* Current trends in craniofacial reconstruction. *The Surgeon* **21**, e118–e125 (2023).

27. Borba, A. M. *et al.* Predictors of complication for alveolar cleft bone graft. *Br. J. Oral Maxillofac. Surg.* **52**, 174–178 (2014).

28. Li, N. *et al*. Advances in biomaterials for oral-maxillofacial bone regeneration: spotlight on periodontal and alveolar bone strategies. *Regen*. *Biomater*. **11**, rbae078 (2024).

29. Ko, F. C. & Sumner, D. R. How faithfully does intramembranous bone regeneration recapitulate embryonic skeletal development? *Dev*. *Dyn*. *Off*. *Publ*. *Am*. *Assoc*. *Anat*. **250**, 377–392 (2021).

30. Szymanska, E., Budick-Harmelin, N. & Miaczynska, M. Endosomal 'sort' of signaling control: The role of ESCRT machinery in regulation of receptor-mediated signaling pathways. *Semin*. *Cell Dev*. *Biol*. https://doi.org/10.1016/j.semcdb.2017.08.012 (2017) doi:10.1016/j.semcdb.2017.08.012.

31. Huotari, J. & Helenius, A. Endosome maturation. *EMBO J*. **30**, 3481–3500 (2011).

32. Christ, L., Raiborg, C., Wenzel, E. M., Campsteijn, C. & Stenmark, H. Cellular Functions and Molecular Mechanisms of the ESCRT Membrane-Scission Machinery. *Trends Biochem*. *Sci*. **42**, 42–56 (2017).

33. Hurley, J. H., Coyne, A. N., Miączyńska, M. & Stenmark, H. The expanding repertoire of ESCRT functions in cell biology and disease. *Nature* **642**, 877–888 (2025).

34. McCullough, J., Frost, A. & Sundquist, W. I. Structures, Functions, and Dynamics of ESCRT-III/Vps4 Membrane Remodeling and Fission Complexes. *Annu*. *Rev*. *Cell Dev*. *Biol*. **34**, 85–109 (2018).

35. Henne, W. M., Stenmark, H. & Emr, S. D. Molecular mechanisms of the membrane sculpting ESCRT pathway. *Cold Spring Harb*. *Perspect*. *Biol*. **5**, a016766 (2013).

36. McCullough, J., Frost, A. & Sundquist, W. I. Structures, Functions, and Dynamics of ESCRT-III/Vps4 Membrane Remodeling and Fission Complexes. *Annu*. *Rev*. *Cell Dev*. *Biol*. **34**, 85–109 (2018).

37. Frankel, E. B. *et al*. Ist1 regulates ESCRT-III assembly and function during multivesicular endosome biogenesis in Caenorhabditis elegans embryos. *Nat*. *Commun*. **8**, 1439 (2017).

38. König, J., Frankel, E. B., Audhya, A. & Müller-Reichert, T. Membrane remodeling during embryonic abscission in Caenorhabditis elegans. *J*. *Cell Biol*. **216**, 1277–1286 (2017).

39. Djeddi, A. *et al*. Induction of autophagy in ESCRT mutants is an adaptive response for cell survival in C. elegans. *J*. *Cell Sci*. **125**, 685–694 (2012).

40. Bauer, I., Brune, T., Preiss, R. & Kölling, R. Evidence for a Nonendosomal Function of the Saccharomyces cerevisiae ESCRT-III-Like Protein Chm7. *Genetics* **201**, 1439–1452 (2015).

41. Vaccari, T. & Bilder, D. The Drosophila tumor suppressor vps25 prevents nonautonomous overproliferation by regulating notch trafficking. *Dev. Cell* **9**, 687–698 (2005).

42. Komada, M. & Soriano, P. Hrs, a FYVE finger protein localized to early endosomes, is implicated in vesicular traffic and required for ventral folding morphogenesis. *Genes Dev.* **13**, 1475–1485 (1999).

43. Yamada, M. *et al.* Signal-transducing adaptor molecules STAM1 and STAM2 are required for T-cell development and survival. *Mol. Cell. Biol.* **22**, 8648–8658 (2002).

44. Ruland, J. *et al.* p53 accumulation, defective cell proliferation, and early embryonic lethality in mice lacking tsg101. *Proc. Natl. Acad. Sci. U. S. A.* **98**, 1859–1864 (2001).

45. Wagner, K.-U. *et al.* Tsg101 is essential for cell growth, proliferation, and cell survival of embryonic and adult tissues. *Mol. Cell. Biol.* **23**, 150–162 (2003).

46. Handschuh, K. *et al.* ESCRT-II/Vps25 constrains digit number by endosome-mediated selective modulation of FGF-SHH signaling. *Cell Rep.* **9**, 674–687 (2014).

47. Jung, E., Choi, T.-I., Lee, J.-E., Kim, C.-H. & Kim, J. ESCRT subunit CHMP4B localizes to primary cilia and is required for the structural integrity of the ciliary membrane. *FASEB J. Off. Publ. Fed. Am. Soc. Exp. Biol.* **34**, 1331–1344 (2020).

48. Zhou, Y., Bennett, T. M. & Shiels, A. A charged multivesicular body protein (CHMP4B) is required for lens growth and differentiation. *Differ. Res. Biol. Divers.* **109**, 16–27 (2019).

49. Chen, D. *et al.* VPS4B deficiency causes early embryonic lethality and induces signal transduction disorders of cell endocytosis. *Genes. N. Y. N 2000* **59**, e23415 (2021).

50. Shim, J.-H. *et al.* CHMP5 is essential for late endosome function and down-regulation of receptor signaling during mouse embryogenesis. *J. Cell Biol.* **172**, 1045–1056 (2006).

51. Isaioglou, I. *et al.* Recessive variants in ESCRT-II component VPS25 alter vesicular transport and small extracellular vesicles processing in lethal neonatal encephalopathy. *Genome Medicine* **18**, 165 (2026).

951 52. Hermosilla Aguayo, V. *et al*. ESCRT-dependent control of craniofacial
952 morphogenesis with concomitant perturbation of NOTCH signaling. *Dev. Biol*. **503**, 25–42
953 (2023).

954 53. Groza, T. *et al*. The International Mouse Phenotyping Consortium: comprehensive
955 knockout phenotyping underpinning the study of human disease. *Nucleic Acids Res*. **51**,
956 D1038–D1045 (2023).

957 54. Zhang, F. *et al*. The ESCRT protein CHMP5 restricts bone formation by controlling
958 endolysosome-mitochondrion-mediated cell senescence. *eLife* **13**, RP101984 (2025).

959 55. Gaytan, F., Morales, C., Reymundo, C. & Tena-Sempere, M. A novel RGB-trichrome
960 staining method for routine histological analysis of musculoskeletal tissues. *Sci. Rep*. **10**,
961 16659 (2020).

962 56. Bolger, J. T. Heterotopic bone formation and alkaline phosphatase. *Arch. Phys. Med.*
963 *Rehabil*. **56**, 36–39 (1975).

964 57. Komori, T. Regulation of Proliferation, Differentiation and Functions of Osteoblasts
965 by Runx2. *Int. J. Mol. Sci*. **20**, 1694 (2019).

966 58. Losa, M. *et al*. Face morphogenesis is promoted by Pbx-dependent EMT via
967 regulation of Snail1 during frontonasal prominence fusion. *Dev. Camb. Engl*. **145**, (2018).

968 59. Ruest, L.-B. *et al*. dHAND-Cre transgenic mice reveal specific potential functions of
969 dHAND during craniofacial development. *Dev. Biol*. **257**, 263–277 (2003).

970 60. Bush, J. O. & Jiang, R. Palatogenesis: morphogenetic and molecular mechanisms of
971 secondary palate development. *Development* **139**, 231–243 (2012).

972 61. Miura, H., Quadros, R. M., Gurumurthy, C. B. & Ohtsuka, M. Easi-CRISPR for creating
973 knock-in and conditional knockout mouse models using long ssDNA donors. *Nat. Protoc.*
974 **13**, 195–215 (2018).

975 62. Quadros, R. M. *et al*. Easi-CRISPR: a robust method for one-step generation of mice
976 carrying conditional and insertion alleles using long ssDNA donors and CRISPR
977 ribonucleoproteins. *Genome Biol*. **18**, 92 (2017).

978 63. Reid, B. S., Yang, H., Melvin, V. S., Taketo, M. M. & Williams, T. Ectodermal Wnt/β-
979 catenin signaling shapes the mouse face. *Dev. Biol*. **349**, 261–269 (2011).

980 64. Schock, E. N. *et al*. A tissue-specific role for intraflagellar transport genes during
981 craniofacial development. *PloS One* **12**, e0174206 (2017).

65. Lewis, A. E., Vasudevan, H. N., O'Neill, A. K., Soriano, P. & Bush, J. O. The widely used Wnt1-Cre transgene causes developmental phenotypes by ectopic activation of Wnt signaling. *Dev. Biol.* **379**, 229–234 (2013).

66. Prigge, J. R. *et al.* Nuclear double-fluorescent reporter for in vivo and ex vivo analyses of biological transitions in mouse nuclei. *Mamm. Genome Off. J. Int. Mamm. Genome Soc.* https://doi.org/10.1007/s00335-013-9469-8 (2013) doi:10.1007/s00335-013-9469-8.

67. Dougherty, K. J. *et al.* Locomotor rhythm generation linked to the output of spinal shox2 excitatory interneurons. *Neuron* **80**, 920–933 (2013).

68. Lefebvre, V. & Dvir-Ginzberg, M. SOX9 and the many facets of its regulation in the chondrocyte lineage. *Connect. Tissue Res.* **58**, 2–14 (2017).

69. Xavier, G. M., Miletich, I. & Cobourne, M. T. Ephrin Ligands and Eph Receptors Show Regionally Restricted Expression in the Developing Palate and Tongue. *Front. Physiol.* **7**, 60 (2016).

70. Qu, T. *et al.* Cell Cycle Arrest of a 'Zippering' Epithelial Cell Cluster Shapes the Face and is Disrupted in Craniofacial Disorders. *bioRxiv* 2025.07.28.667310 (2025) doi:10.1101/2025.07.28.667310.

71. J, S., Cs, R. & P, S. PDGF signaling specificity is mediated through multiple immediate early genes. *Nat. Genet.* **39**, (2007).

72. Hata, K. *et al.* Arid5b facilitates chondrogenesis by recruiting the histone demethylase Phf2 to Sox9-regulated genes. *Nat. Commun.* **4**, 2850 (2013).

73. Kiepe, D., Ciarmatori, S., Hoeflich, A., Wolf, E. & Tönshoff, B. Insulin-Like Growth Factor (IGF)-I Stimulates Cell Proliferation and Induces IGF Binding Protein (IGFBP)-3 and IGFBP-5 Gene Expression in Cultured Growth Plate Chondrocytes via Distinct Signaling Pathways. *Endocrinology* **146**, 3096–3104 (2005).

74. Horner, D. S. *et al.* ESCRT genes and regulation of developmental signaling. *Semin. Cell Dev. Biol.* https://doi.org/10.1016/j.semcdb.2017.08.038 (2017) doi:10.1016/j.semcdb.2017.08.038.

75. Seghatoleslami, M. R. *et al.* Differential regulation of COL2A1 expression in developing and mature chondrocytes. *Matrix Biol.* **14**, 753–764 (1995).

76. Komori, T. Runx2, an inducer of osteoblast and chondrocyte differentiation. *Histochem. Cell Biol.* **149**, 313–323 (2018).

77. Zhou, X. *et al.* PQ401, an IGF-1R inhibitor, induces apoptosis and inhibits growth, proliferation and migration of glioma cells. *J. Chemother.* **28**, 44–49 (2016).

78. Qi, B. *et al.* IGF-1R inhibitor PQ401 inhibits osteosarcoma cell proliferation, migration and colony formation. *Int. J. Clin. Exp. Pathol.* **12**, 1589–1598 (2019).

79. Hutchison, M. R., Bassett, M. H. & White, P. C. Insulin-like growth factor-I and fibroblast growth factor, but not growth hormone, affect growth plate chondrocyte proliferation. *Endocrinology* **148**, 3122–3130 (2007).

80. Heilig, J., Paulsson, M. & Zaucke, F. Insulin-like growth factor 1 receptor (IGF1R) signaling regulates osterix expression and cartilage matrix mineralization during endochondral ossification. *Bone* **83**, 48–57 (2016).

81. Phornphutkul, C., Wu, K.-Y., Yang, X., Chen, Q. & Gruppuso, P. A. Insulin-like growth factor-I signaling is modified during chondrocyte differentiation. *J. Endocrinol.* **183**, 477–486 (2004).

82. Cooper, K. L. *et al.* Multiple phases of chondrocyte enlargement underlie differences in skeletal proportions. *Nature* **495**, 375–378 (2013).

83. Wang, J., Zhou, J. & Bondy, C. A. Igf1 promotes longitudinal bone growth by insulin-like actions augmenting chondrocyte hypertrophy. *FASEB J.* **13**, 1985–1990 (1999).

84. Hayashi, S. & McMahon, A. P. Efficient recombination in diverse tissues by a tamoxifen-inducible form of Cre: a tool for temporally regulated gene activation/inactivation in the mouse. *Dev. Biol.* **244**, 305–318 (2002).

85. Murillo-Rincón, A. P. *et al.* Positional programs in early murine facial development and their role in human facial shape variability. *Nat. Commun.* **16**, 10112 (2025).

86. Hierro, A. *et al.* Structure of the ESCRT-II endosomal trafficking complex. *Nature* **431**, 221–225 (2004).

87. Malerød, L., Stuffers, S., Brech, A. & Stenmark, H. Vps22/EAP30 in ESCRT-II mediates endosomal sorting of growth factor and chemokine receptors destined for lysosomal degradation. *Traffic Cph. Den.* **8**, 1617–1629 (2007).

88. Bowers, K. *et al.* Degradation of endocytosed epidermal growth factor and virally ubiquitinated major histocompatibility complex class I is independent of mammalian ESCRTII. *J. Biol. Chem.* **281**, 5094–5105 (2006).

89. Brugger, M. *et al.* Bi-allelic variants in SNF8 cause a disease spectrum ranging from severe developmental and epileptic encephalopathy to syndromic optic atrophy. *Am. J. Hum. Genet.* **111**, 594–613 (2024).

90. Cesario, J. M. *et al.* Anti-osteogenic function of a LIM-homeodomain transcription factor LMX1B is essential to early patterning of the calvaria. *Dev. Biol.* **443**, 103–116 (2018).

91. Economou, M. A. *et al.* Oral Picropodophyllin (PPP) Is Well Tolerated In Vivo and Inhibits IGF-1R Expression and Growth of Uveal Melanoma. *Invest. Ophthalmol. Vis. Sci.* **49**, 2337–2342 (2008).

92. Tarnowski, M. *et al.* Picropodophyllin (PPP) is a potent rhabdomyosarcoma growth inhibitor both in vitro and in vivo. *BMC Cancer* **17**, 532 (2017).

93. Sekar, R. *et al.* Vps37a regulates hepatic glucose production by controlling glucagon receptor localization to endosomes. *Cell Metab.* **34**, 1824-1842.e9 (2022).

94. Fukuda, M. Lysosomal membrane glycoproteins. Structure, biosynthesis, and intracellular trafficking. *J. Biol. Chem.* **266**, 21327–21330 (1991).

95. Vecchione, A., Marchese, A., Henry, P., Rotin, D. & Morrione, A. The Grb10/Nedd4 complex regulates ligand-induced ubiquitination and stability of the insulin-like growth factor I receptor. *Mol. Cell. Biol.* **23**, 3363–3372 (2003).

96. Yuan, Y. & Chai, Y. Regulatory mechanisms of jaw bone and tooth development. *Curr. Top. Dev. Biol.* **133**, 91–118 (2019).

97. Michelet, X., Djeddi, A. & Legouis, R. Developmental and cellular functions of the ESCRT machinery in pluricellular organisms. *Biol. Cell* **102**, 191–202 (2010).

98. Vietri, M., Radulovic, M. & Stenmark, H. The many functions of ESCRTs. *Nat. Rev. Mol. Cell Biol.* **21**, 25–42 (2020).

99. Colozza, G. *et al.* Wnt-inducible Lrp6-APEX2 interacting proteins identify ESCRT machinery and Trk-fused gene as components of the Wnt signaling pathway. *Sci. Rep.* **10**, 21555 (2020).

100. Miller, D. S. J. *et al.* The Dynamics of TGF-β Signaling Are Dictated by Receptor Trafficking via the ESCRT Machinery. *Cell Rep.* **25**, 1841-1855.e5 (2018).

101. Rieger, L. & O'Connor, R. Controlled Signaling—Insulin-Like Growth Factor Receptor Endocytosis and Presence at Intracellular Compartments. *Front. Endocrinol.* **11**, 620013 (2021).

102. Marmor, Md. & Yarden, Y. Role of protein ubiquitylation in regulating endocytosis of receptor tyrosine kinases. *Oncogene* **23**, (2004).

103. Sehat, B., Andersson, S., Vasilcanu, R., Girnita, L. & Larsson, O. Role of ubiquitination in IGF-1 receptor signaling and degradation. *PloS One* **2**, e340 (2007).

104. Sehat, B., Andersson, S., Girnita, L. & Larsson, O. Identification of c-Cbl as a new ligase for insulin-like growth factor-I receptor with distinct roles from Mdm2 in receptor ubiquitination and endocytosis. *Cancer Res.* **68**, 5669–5677 (2008).

105. Yoneyama, Y. *et al.* IRS-1 acts as an endocytic regulator of IGF-I receptor to facilitate sustained IGF signaling. *eLife* **7**, e32893 (2018).

106. Humphreys, R. *et al.* Cranial neural crest ablation of Jagged1 recapitulates the craniofacial phenotype of Alagille syndrome patients. *Hum. Mol. Genet.* **21**, 1374–1383 (2012).

107. Kamath, B. M. *et al.* NOTCH2 mutations in Alagille syndrome. *J. Med. Genet.* **49**, 138–144 (2012).

108. Esposito, A., Klüppel, M., Wilson, B. M., Meka, S. R. K. & Spagnoli, A. CXCR4 mediates the effects of IGF-1R signaling in rodent bone homeostasis and fracture repair. *Bone* **166**, 116600 (2023).

109. Xing, W., Kesavan, C., Pourteymoor, S. & Mohan, S. Global and Conditional Disruption of the Igf-I Gene in Osteoblasts and/or Chondrocytes Unveils Epiphyseal and Metaphyseal Bone-Specific Effects of IGF-I in Bone. *Biology* **12**, 1228 (2023).

110. Zhang, M. *et al.* Osteoblast-specific knockout of the insulin-like growth factor (IGF) receptor gene reveals an essential role of IGF signaling in bone matrix mineralization. *J. Biol. Chem.* **277**, 44005–44012 (2002).

111. Govoni, K. E. *et al.* Conditional deletion of insulin-like growth factor-I in collagen type 1alpha2-expressing cells results in postnatal lethality and a dramatic reduction in bone accretion. *Endocrinology* **148**, 5706–5715 (2007).

112. Govoni, K. E. *et al.* Disruption of insulin-like growth factor-I expression in type IIalphaI collagen-expressing cells reduces bone length and width in mice. *Physiol. Genomics* **30**, 354–362 (2007).

113. Ovchinnikov, D. A., Deng, J. M., Ogunrinu, G. & Behringer, R. R. Col2a1-directed expression of Cre recombinase in differentiating chondrocytes in transgenic mice. *Genesis* **26**, 145–146 (2000).

114. Escribano-Núñez, A. *et al*. IGF1 drives Wnt-induced joint damage and is a potential therapeutic target for osteoarthritis. *Nat. Commun.* **15**, 9170 (2024).

115. Chen, Y. *et al*. Insulin-like growth factor-1 boosts the developing process of condylar hyperplasia by stimulating chondrocytes proliferation. *Osteoarthritis Cartilage* **20**, 279–287 (2012).

116. Mao, D. *et al*. Suppression of Overactive Insulin-Like Growth Factor 1 Attenuates Trauma-Induced Heterotopic Ossification in Mice. *Am. J. Pathol.* **194**, 430–446 (2024).

117. Roback, E. W. *et al*. An Infant With Deletion of the Distal Long Arm of Chromosome 15 (q26.1→qter) and Loss of Insulin-Like Growth Factor 1 Receptor Gene. *Am. J. Med. Genet.* **38**, 74–79 (1991).

118. Rump, P. *et al*. Drayer's syndrome of mental retardation, microcephaly, short stature and absent phalanges is caused by a recurrent deletion of chromosome 15(q26.2-->qter). *Clin. Genet.* **74**, 455–462 (2008).

119. Woods, K. A., Camacho-Hübner, C., Savage, M. O. & Clark, A. J. Intrauterine growth retardation and postnatal growth failure associated with deletion of the insulin-like growth factor I gene. *N. Engl. J. Med.* **335**, 1363–1367 (1996).

120. Wang, W., Bian, J., Sun, Y. & Li, Z. The new fate of internalized membrane receptors: Internalized activation. *Pharmacol. Ther.* **233**, 108018 (2022).

121. Miaczynska, M. Effects of membrane trafficking on signaling by receptor tyrosine kinases. *Cold Spring Harb. Perspect. Biol.* **5**, a009035 (2013).

122. Hudacova, E. *et al*. Single-cell transcriptomic resolution of osteogenesis during craniofacial morphogenesis. *Bone* **190**, 117297 (2025).

123. Hudacova, E., Zucha, D., Kaplan, M. M. & Machon, O. Meis2 transcription factor regulates craniofacial osteogenesis via IGF signaling and cell adhesion. *Bone* **213**, 118075 (2026).

124. Babst, M., Katzmann, D. J., Snyder, W. B., Wendland, B. & Emr, S. D. Endosome-associated complex, ESCRT-II, recruits transport machinery for protein sorting at the multivesicular body. *Dev. Cell* **3**, 283–289 (2002).

125. Park, J., Kim, J., Park, H., Kim, T. & Lee, S. ESCRT-III: a versatile membrane remodeling machinery and its implications in cellular processes and diseases. *Anim. Cells Syst.* **28**, 367–380 (2024).

126. McCullough, J. *et al.* Structure and membrane remodeling activity of ESCRT-III helical polymers. *Science* **350**, 1548–1551 (2015).

127. Jukic, N., Perrino, A. P., Redondo-Morata, L. & Scheuring, S. Structure and dynamics of ESCRT-III membrane remodeling proteins by high-speed atomic force microscopy. *J. Biol. Chem.* **299**, 104575 (2023).

128. Shankar, R., Lettman, M. M., Whisler, W., Frankel, E. B. & Audhya, A. The ESCRT machinery directs quality control over inner nuclear membrane architecture. *Cell Rep.* **38**, 110263 (2022).

129. Casares-Arias, J. *et al.* Midbody Remnant Inheritance Is Regulated by the ESCRT Subunit CHMP4C. *iScience* **23**, 101244 (2020).

130. Umphred-Wilson, K. *et al.* The ESCRT protein CHMP5 promotes T cell leukemia by enabling BRD4-p300-dependent transcription. *Nat. Commun.* **16**, 4133 (2025).

131. García-García, M. J. *et al.* Analysis of mouse embryonic patterning and morphogenesis by forward genetics. *Proc. Natl. Acad. Sci. U. S. A.* **102**, 5913–5919 (2005).

132. Lewandoski, M., Meyers, E. N. & Martin, G. R. Analysis of Fgf8 gene function in vertebrate development. *Cold Spring Harb. Symp. Quant. Biol.* **62**, 159–168 (1997).

133. Bernar, A., Gebetsberger, J. V., Bauer, M., Streif, W. & Schirmer, M. Optimization of the Alizarin Red S Assay by Enhancing Mineralization of Osteoblasts. *Int. J. Mol. Sci.* **24**, 723 (2022).

134. Feoktistova, M., Geserick, P. & Leverkus, M. Crystal Violet Assay for Determining Viability of Cultured Cells. *Cold Spring Harb. Protoc.* **2016**, pdb.prot087379 (2016).

135. Nagy, A., Gertsenstein, M., Vintersten, K. & Behringer, R. Alcian blue staining of the mouse fetal cartilaginous skeleton. *Cold Spring Harb. Protoc.* **2009**, pdb.prot5169 (2009).

136. Galaxy Community. Galaxy for accessible, reproducible, and collaborative data analyses: 2026 update. *Nucleic Acids Res.* **54**, W105–W116 (2026).

137. Elizarraras, J. M. *et al.* WebGestalt 2024: faster gene set analysis and new support for metabolomics and multi-omics. *Nucleic Acids Res.* **52**, W415–W421 (2024).

138. Schindelin, J. *et al.* Fiji: an open-source platform for biological-image analysis. *Nat. Methods* **9**, 676–682 (2012).

AUTHOR CONTRIBUTIONS

L.S. supervised the project, provided funding, and obtained patients' fibroblasts from affected children carrying biallelic *VPS25* variants. V.H.A. conceived the project, led the design of all experimental procedures and conducted all data analyses, including preparation of RNAseq libraries and bioinformatics. J.d.A. assisted with mouse colony maintenance, genotyping, sample collection, cryosectioning, immunofluorescence, and cell culture. M.R. and V.H.A. conducted flow cytometry. M.R. advised on bioinformatic analysis. M.O.H, S.H., and L.A. obtained skin biopsies from healthy donors and patients harboring *VPS25* variants and isolated primary fibroblasts that were shipped to UCSF. V.H.A. and L.S. contributed to manuscript writing and editing. All authors read the manuscript and agreed with the submitted version.

COMPETING INTERESTS

The authors declare no competing interests.

FUNDING

This work was supported by the National Institute of Dental and Craniofacial Research (NIDCR) Grants R01 DE033885 and R01 DE028753 to L.S. The UCSF Center for Advanced Technology (CAT) was supported by UCSF PBBR, RRP IMIA, and NIH 1S10OD028511-01 grants. V.H.A. was recipient of the Tobacco-Related Disease Research Program (TRDRP) Postdoctoral Fellowship #T32FT4997; the American Association of University Women (AAUW) International Fellowship; and the Program for Breakthrough Biomedical Research (PBBR) Postdoc Independent Research Grant. In addition, V.H.A. is grateful to Dr. Caroline H. Damsky for the "Damsky Exploratory Grants Initiative" award and to the Wu-McClain family for the endowed fellowship.

DATA AVAILABILITY

All data supporting the findings described in this manuscript are available in the article, its Supplementary data files, or from the corresponding authors upon request (Licia Selleri, Licia.Selleri@ucsf.edu; Viviana Hermosilla Aguayo, Viviana.hermosillaaguayo@ucsf.edu). Bulk RNA-seq raw data are available at GEO repository (accession number GSE351768).

ETHICS

Family of 21DG0856 (*VPS25*:NM_032353.3:c.23C>T;c.514G>A) was recruited under institutional review board (IRB)-approved research protocol EK 1115/2024. Families of 25DG0089 and 25DG339 (*VPS25*:NM_032353.4:c.22C>T) were identified through Lifera Omics Database and recruited under IRB-approved research protocol KFSHRC RAC# 2121053 and 2210029. Control fibroblast cell cultures were established from circumcision procedures from seemingly healthy males recruited under IRB-approved research protocol KFSHRC RAC# 2110023. All experiments were performed in accordance with relevant guidelines and regulations at the respective institutions. Written informed consent was obtained from the parents/legal guardians. The research conformed to the principles of the Declaration of Helsinki.

All animal procedures complied with institutional guidelines for animal care and were carried out under protocol AN205176-00E, approved by the University of California, San Francisco Institutional Animal Care and Use Committee (IACUC).

ACKNOWLEDGEMENTS

We thank the members of the Selleri Laboratory for valuable discussions; Dr. Fowzan S. Alkuraya for his assistance in obtaining human primary fibroblasts and for providing insight into the childhood *VPS25* syndrome; Mr. Robert Aho for quantification of

proliferation and apoptosis assays; Miss Erika Moskewicz for western blot analysis;Dr. Erica Hutchins for making the confocal microscope available; Dr. Andrew Brack for sharing the *R26R*^{nTnG} mouse line; the University of Michigan Transgenic Animal Model Core for the *Vps25* conditional allele; and the UCSF Center for Advanced Technology(CAT) for high-throughput sequencing.

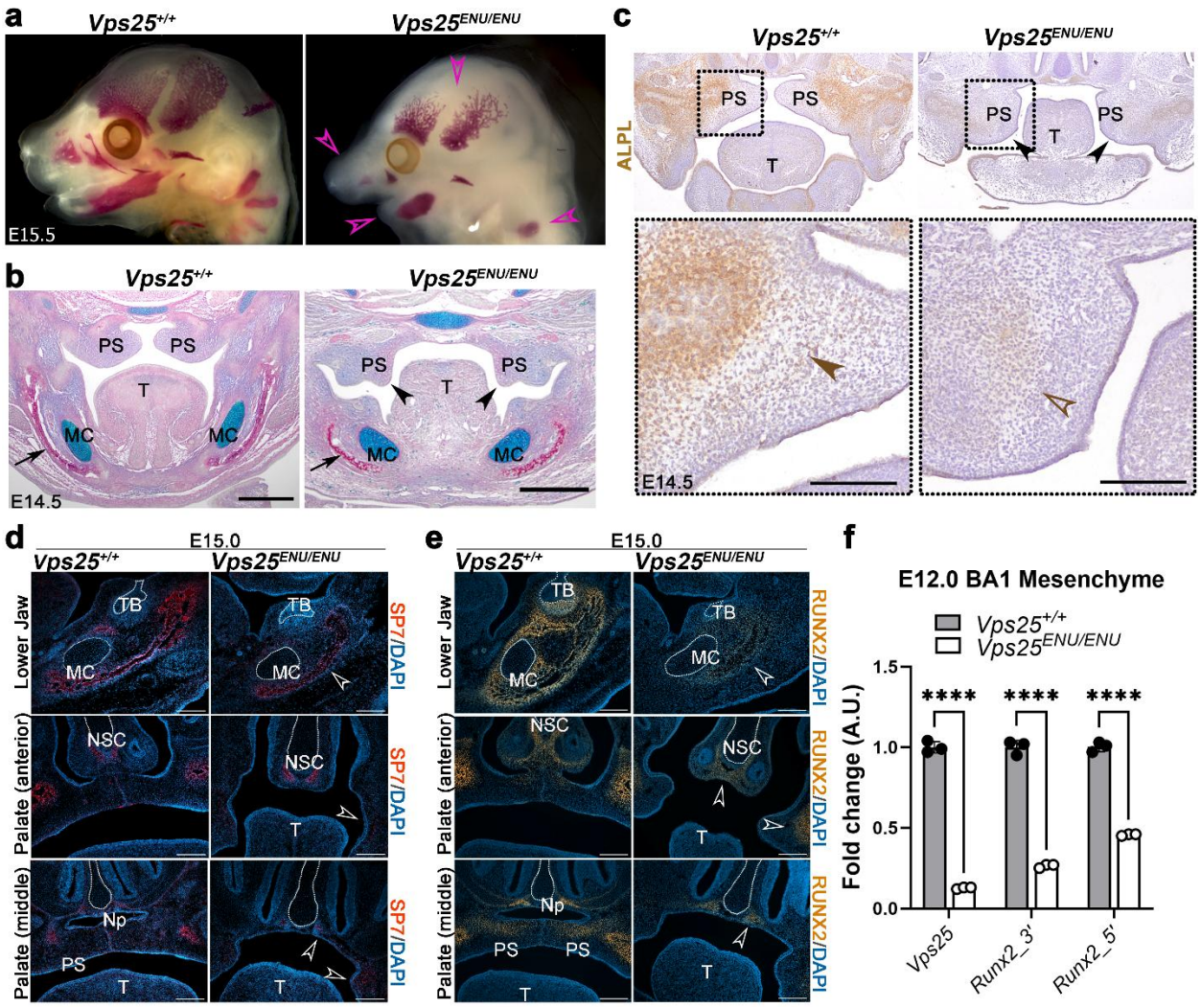


Figure 1. Defective craniofacial bone formation and secondary palatal closure in mice with hypomorphic loss of *Vps25*. (a) Alizarin red staining visualizes upper and lower jaw bones as well as calvarial bones and cervical vertebrae (right; empty magenta arrowheads) of *Vps25*$^{ENU/ENU}$ embryo *versus* wildtype control (left). **(b)** RGB-trichrome-stained coronal sections from E14.5 wildtype (*Vps25*$^{+/+}$) and *Vps25* mutant (*Vps25*$^{ENU/ENU}$) heads. Black arrowheads point to defective elevation of palatal shelves (PS) on the sides of the tongue (T) in *Vps25*$^{ENU/ENU}$ embryos. Sirius red staining (dark pink) around Meckel's cartilage rods (MC, blue) denotes bone formation in lower jaw (black arrows). Scale bar=500 μm. **(c)** Alkaline phosphatase (ALPL) immunohistochemistry in E14.5 coronal sections. Insets (bottom panels) show higher magnification of PS, with drastically decreased ALPL immunostaining observed in *Vps25* mutant embryo (right; empty brown arrowhead) *versus* control (left; solid brown arrowhead). Scale bar=200 μm. **(d)** SP7 (red) and **(e)** RUNX2 (orange) immunofluorescence in coronal sections comprising lower jaw, as well as anterior and middle secondary palate of E15.0 wildtype and *Vps25* mutant embryos. Decreased staining of SP7 and RUNX2 bone markers in mutant craniofacial domains highlighted by white empty arrowheads. DAPI: DNA, blue. NSC; nasal septum cartilage; TB; tooth bud; Np; nasopharynx. Dotted white lines outline cartilage tissue and TB Scale bar=200 μm.

(f) qRT-PCR quantification of *Vps25* and *Runx2* transcript levels in Branchial Arch 1 (BA1) mesenchyme from E12.0 wildtype and *Vps25* mutant embryos. Error bars=SD. Two-way ANOVA with Šidák multiple comparisons test. p value ≤ 0.0001=****.

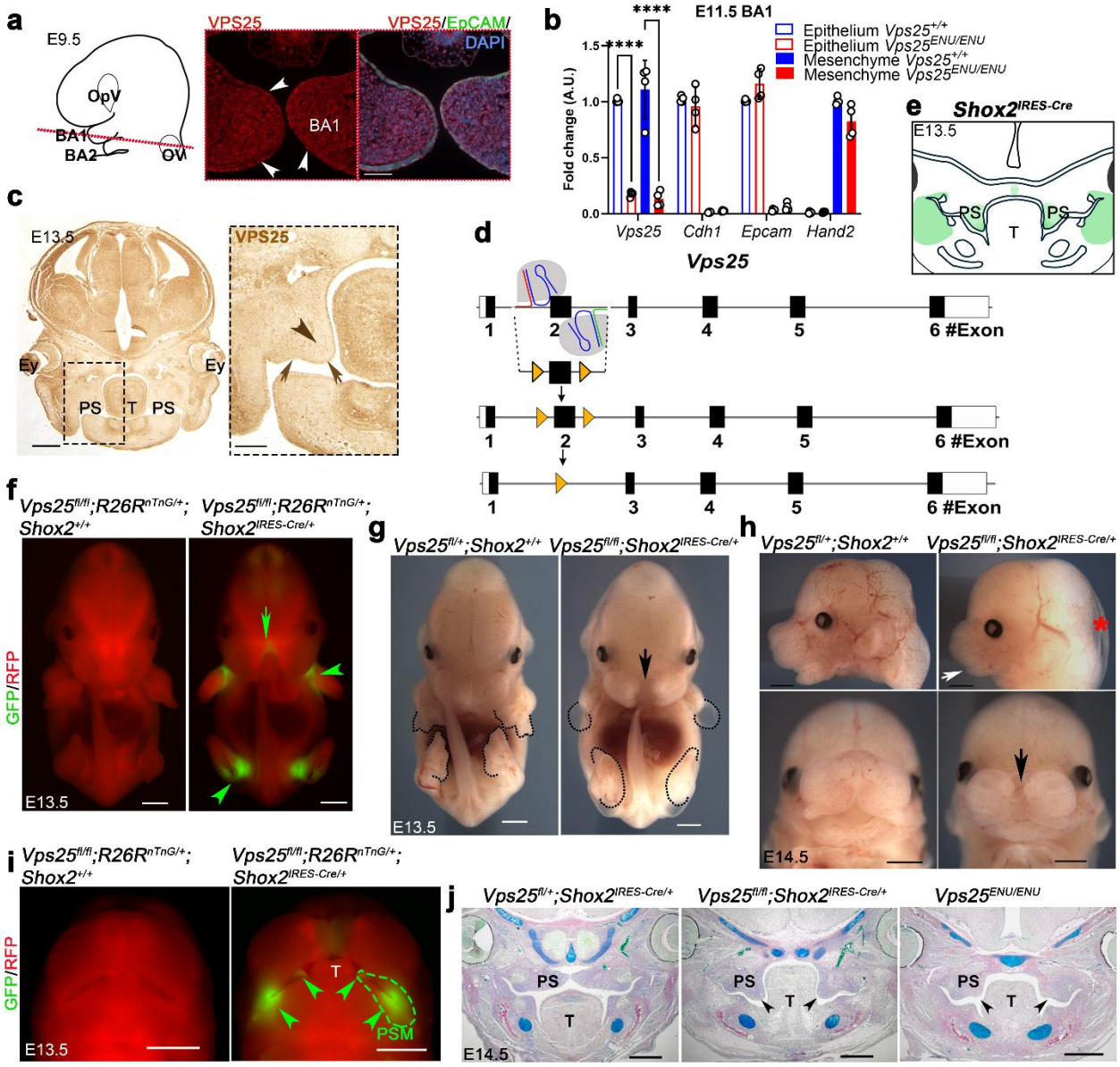


Figure 2. *Vps25* mesenchymal-specific loss causes split face and failed secondary palate elevation. (a) VPS25 (red) and EpCAM (epithelium, green) immunofluorescence in E9.5 wildtype murine transverse sections, schematized in left panel. DAPI: DNA, blue. BA1, BA2; Branchial Arch 1 and 2. OV; Otic vesicle. OpV; Optic vesicle. Scale bar=100 μm. **(b)** qRT-PCR of *Vps25*, *Cdh1, Epcam,* and *Hand2* in epithelium and mesenchyme of E11.5 wildtype and *Vps25* mutant BA1. Error bars=SD. Two-way ANOVA with Tukey's post-test. p value ≤ 0.0001=****. **(c)** VPS25 immunohistochemistry in E13.5 wildtype coronal sections. Brown arrows and arrowheads point to signal in palatal shelf (PS) epithelium and mesenchyme, respectively. Ey; eye. T; tongue. Scale bar=500 μm. Inset bar=200 μm. **(d)** Schematic of *Vps25* conditional allele. Exon 2 flanked by *loxP* sites (yellow triangles); ribonucleoprotein complex comprising guide RNAs (hairpins) and Cas9 (grey bubble); *Cre*-mediated recombination leads to Exon 2 excision (bottom). **(e)** Representation of Cre activity (green areas) in coronal sections from E13.5 *Shox2*$^{IRES\text{-}Cre}$ embryo. **(f)** Frontal views of E13.5 *Vps25*$^{fl/fl}$;*R26R*$^{nTnG/+}$;*Shox2*$^{+/+}$ and *Vps25*$^{fl/fl}$;*R26R*$^{nTnG/+}$;*Shox2*$^{IRES\text{-}}$

$^{Cre/+}$ embryos. Mesenchymal limb and face tissues harboring *Shox2-Cre* mediated *Vps25* deletion visualized in green (GPF+, green arrow and arrowheads). Tissues devoid of Cre activity remain RFP+ (red). Scale bar=1 mm. **(g)** Frontal views of *Cre* negative control embryos (*Vps25*$^{fl/fl}$*;Shox2*$^{+/+}$) and mutants with *Vps25* homozygous mesenchymal loss (*Vps25*$^{fl/fl}$*;Shox2*$^{IRES\text{-}Cre/+}$). *Vps25* inactivation in limb bud mesenchyme results in abnormal morphology (dotted black lines). *Vps25* loss in facial mesenchyme leads to cleft face (black arrow). Scale bar=1 mm. **(h)** Lateral (top) and frontal (bottom) views of E14.5 embryonic heads with *Vps25* homozygous loss (*Vps25*$^{fl/fl}$*;Shox2*$^{IRES\text{-}Cre/+}$) in facial mesenchyme displaying hypoplastic lower jaw (white arrow), cleft face (black arrow) and edema (red asterisk) *versus* controls (*Vps25*$^{fl/+}$*;Shox2*$^{+/+}$). Scale bar=1 mm. **(i)** Oral views of embryos in **(f)**. Cre reporter activity in PS extending laterally into the maxilla proper (green arrowheads), domain hereafter referred to as PSM. Scale bar=1 mm. **(j)** RGB-trichrome-stained coronal sections from E14.5 embryos with homozygous loss of *Vps25* (*Vps25*$^{fl/fl}$*;Shox2*$^{IRES\text{-}Cre/+}$) in PSM mesenchyme exhibit defective PS elevation (black arrowheads) compared to heterozygous controls (*Vps25*$^{fl/+}$*;Shox2*$^{IRES\text{-}Cre/+}$), mimicking the *Vps25* homozygous hypomorphic phenotype (*Vps25*$^{ENU/ENU}$, right panel). T; tongue. Scale bar=500 μm.

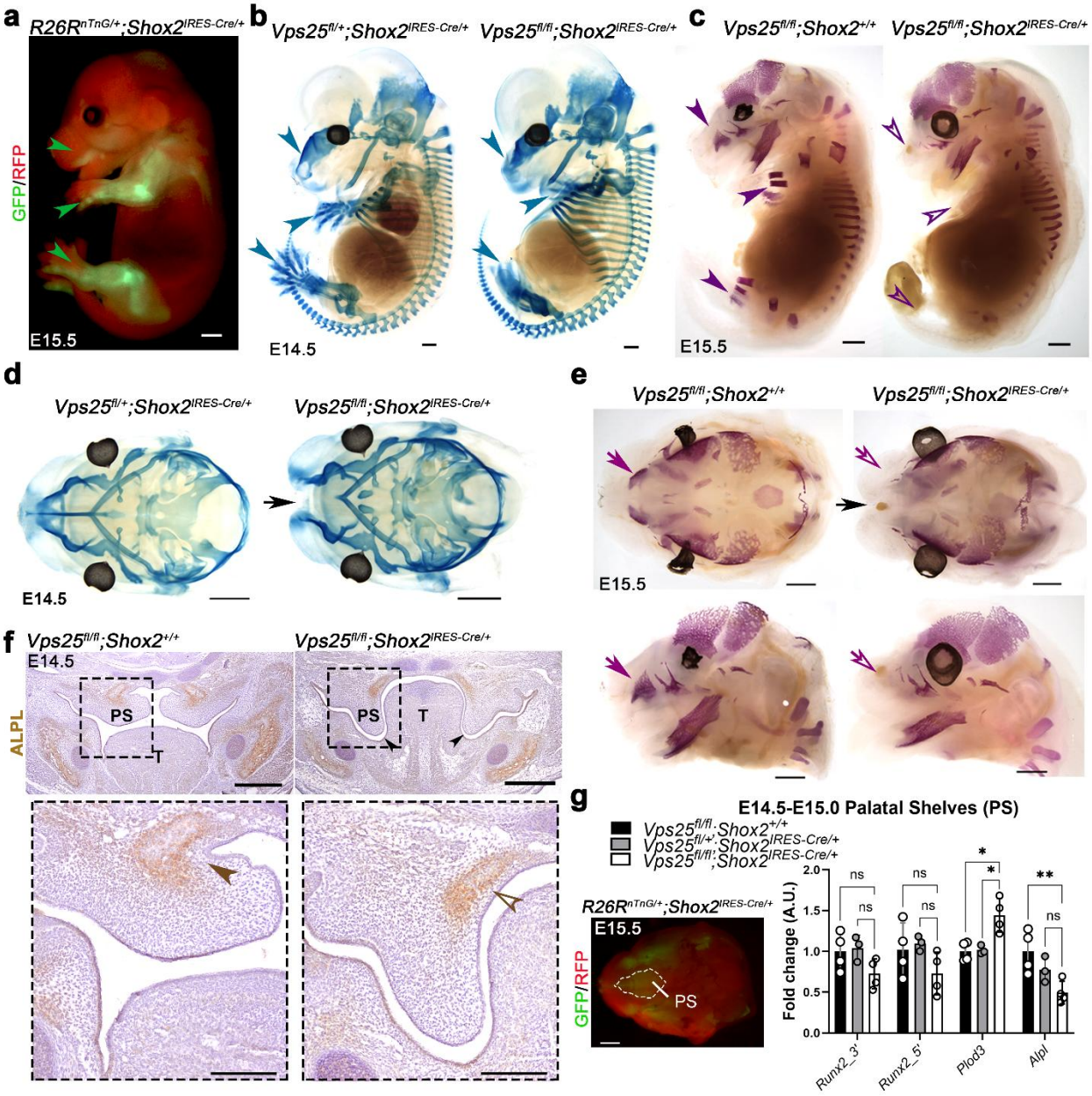


Figure 3. Mesenchymal VPS25 is required for formation of flat and long bones. (a) Visualization of E15.5 embryonic tissues derived from *Cre*+ cells as GFP+ domains (green). Green arrows point to *Cre*+ mesenchyme of upper jaw, forelimbs and hindlimbs. Scale bar=1 mm. **(b)** Alcian blue staining showing cartilaginous structures (snouts and limbs, blue arrowheads) in both E14.5 *Vps25*$^{fl/+}$;*Shox2*$^{IRES\text{-}Cre/+}$ heterozygous controls and *Vps25*$^{fl/fl}$;*Shox2*$^{IRES\text{-}Cre/+}$ homozygous mutant embryos. Scale bar=500 µm. **(c)** Alizarin red staining in *Vps25*$^{fl/fl}$;*Shox2*$^{+/+}$ controls and *Vps25*$^{fl/fl}$;*Shox2*$^{IRES\text{-}Cre/+}$ mutant embryos. E15.5 *Vps25* homozygous mutant embryos are characterized by hypoplastic or absent bones (empty magenta arrowheads) in *Cre*+ domains *versus* controls (solid magenta arrowhead). Scale bar=1 mm. **(d)** Upper view of E14.5 alcian blue-stained heads showing cartilaginous structures in control heterozygous (*Vps25*$^{fl/+}$;*Shox2*$^{IRES\text{-}Cre/+}$) and conditional homozygous mutant (*Vps25*$^{fl/fl}$;*Shox2*$^{IRES\text{-}Cre/+}$) embryos displaying cleft face (black arrow). Scale bar=1 mm. **(e)** Upper (top) and lateral (bottom) views of alizarin red-stained heads from control

(*Vps25*$^{fl/fl}$;*Shox2*$^{+/+}$) and conditional homozygous mutant (*Vps25*$^{fl/fl}$;*Shox2*$^{IRES\text{-}Cre/+}$) embryos with cleft face (black arrow). Premaxillary bone, present in E15.5 controls (solid magenta arrows), is absent in mutant embryos (empty magenta arrows). Scale bar=1 mm. **(f)** Alkaline phosphatase (ALPL) immunohistochemistry in coronal sections from E14.5 embryo with *Vps25* mesenchymal loss (*Vps25*$^{fl/fl}$;*Shox2*$^{IRES\text{-}Cre/+}$) *versus Cre* negative control (*Vps25*$^{fl/fl}$;*Shox2*$^{+/+}$). T; tongue. PS; palatal shelves. Scale bar=500 µm. Insets show higher magnification of ALPL staining in control (solid brown arrowhead) and mutant (empty brown arrowhead) PS. Scale bar=200 µm. **(g)** Left: oral view of PS with GFP signal reporting *Shox2-Cre* activity in E15.5 *R26R*$^{nTnG/+}$;*Shox2*$^{IRES\text{-}Cre\ /+}$ embryo. Tissue collected for qRT-PCR highlighted by dashed white line. Right: qRT-PCR transcript quantification for *Runx2, Plod3*, and *Alpl* in PS from embryos with palatal mesenchyme homozygous *Vps25* loss (*Vps25*$^{fl/fl}$;*Shox2*$^{IRES\text{-}Cre/+}$) *versus* controls (*Vps25*$^{fl/+}$;*Shox2*$^{IRES\text{-}Cre/+}$ or *Vps25*$^{fl/fl}$;*Shox2*$^{+/+}$). Error bars =SD. Two-way ANOVA with Tukey's multiple comparisons test. p value ≤ 0.05=*; p value ≤ 0.01=**. ns=not significant.

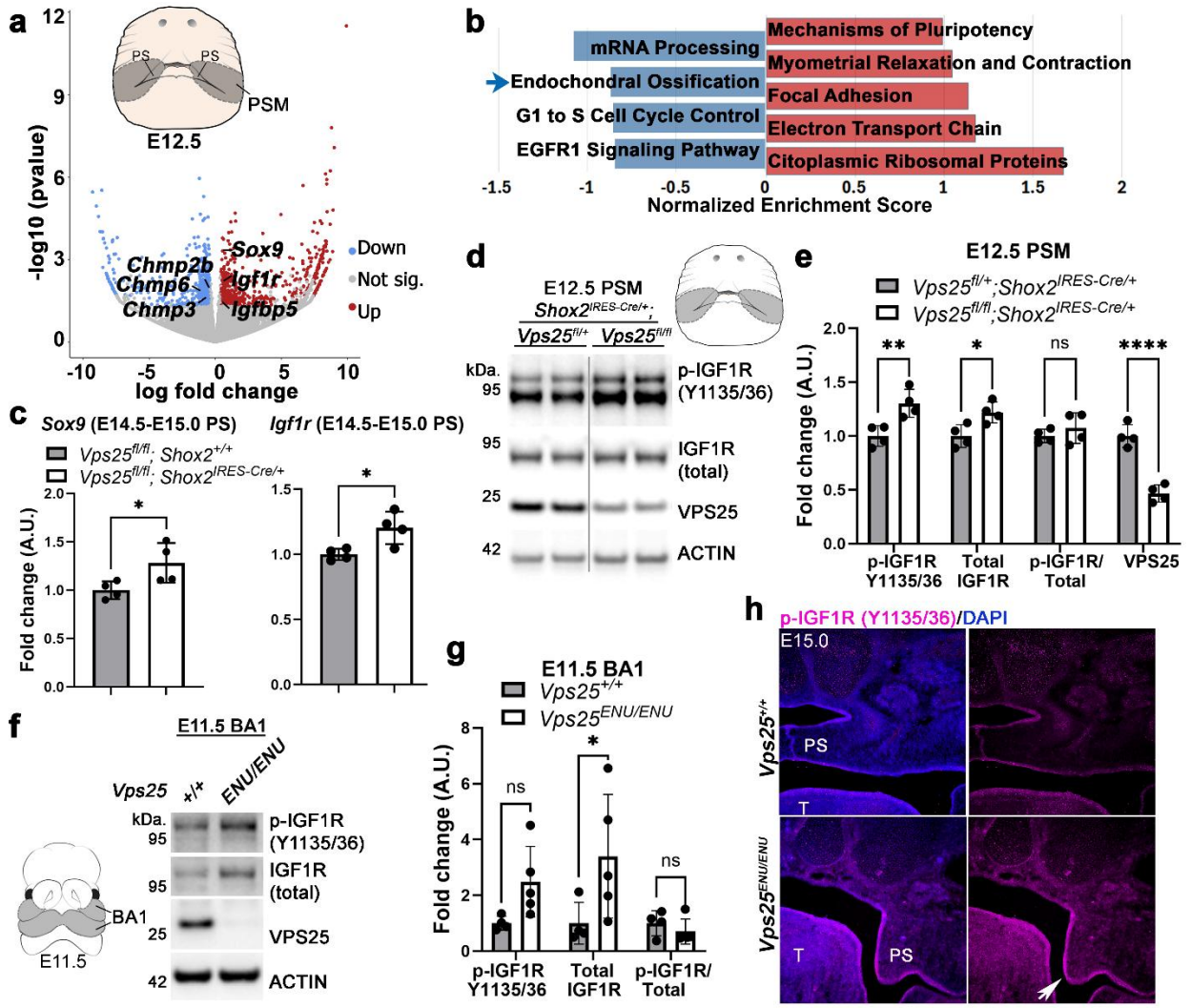


Figure 4. Loss of mesenchymal VPS25 results in aberrant IGF signaling via accumulation of IGF1R. (a) Top: schematic of *Cre*+ PSM comprising maxillary palatal shelf (PS) processes extending laterally into the maxilla proper (grey region), isolated from E12.5 control (*Vps25*$^{+/+}$*;Shox2*$^{IRES\text{-}Cre/+}$) and mutant (*Vps25*$^{fl/fl}$*;Shox2*$^{IRES\text{-}Cre/+}$) embryos for bulk RNA-Seq. Bottom: volcano plot generated from datasets of differentially expressed genes (DEGs) from RNA-Seq analyses. Red and blue dots depict significantly up- and down-regulated genes, respectively, in *Vps25*$^{fl/fl}$*;Shox2*$^{IRES\text{-}Cre/+}$ *versus Vps25*$^{+/+}$*;Shox2*$^{IRES\text{-}Cre/+}$ PSM. **(b)** Pathway analyses of DEGs from RNA-Seq datasets. Terms highlighted in red and blue depict up- and down-regulated pathways, respectively, in *Vps25*$^{fl/fl}$*;Shox2*$^{IRES\text{-}Cre/+}$ compared to *Vps25*$^{+/+}$*;Shox2*$^{IRES\text{-}Cre/+}$ PSM. Blue arrow points to downregulation of endochondral ossification. **(c)** qRT-PCR showing increased expression of *Sox9* (left) and *Igf1r* (right) in PS from *Vps25*$^{fl/fl}$*;Shox2*$^{IRES\text{-}Cre/+}$ embryos *versus Cre* carrier controls. Error bars: SD. Unpaired t-test. p value ≤ 0.05=*. **(d)** Immunoblot of activated IGF1R (p-IGF1R Y1135/36), total IGF1R, VPS25, and Actin in PSM from E12.5 embryos (grey area, schematic on the right) with heterozygous and homozygous conditional *Vps25* loss. **(e)** Quantification of **(d)**. Actin used as loading control. Error bars: SD. Two-way ANOVA with Sidak's multiple comparisons test. p value ≤ 0.05=*; p value ≤ 0.01=**; p value ≤ 0.0001=****; ns= not significant. **(f)** Immunoblot of

activated IGF1R (p-IGF1R Tyr1135/36), total IGF1R, VPS25, and Actin in Branchial Arch 1 (BA1, grey region; schematic on the left) from E11.5 wildtype (*Vps25*$^{+/+}$) and homozygous hypormorphic mutant embryos (*Vps25*$^{ENU/ENU}$). **(g)** Quantification of **(f)**. Error bars: SD. Two-way ANOVA with Sidak's multiple comparisons test. p value ≤ 0.05=*; ns= not significant. **(h)** Immunofluorescence of activated IGF1R (p-Y1135/36, magenta) reveals accumulation of the active phosphorylated receptor in *Vps25*$^{ENU/ENU}$ PS compared to control. DAPI: DNA, blue. T; tongue.

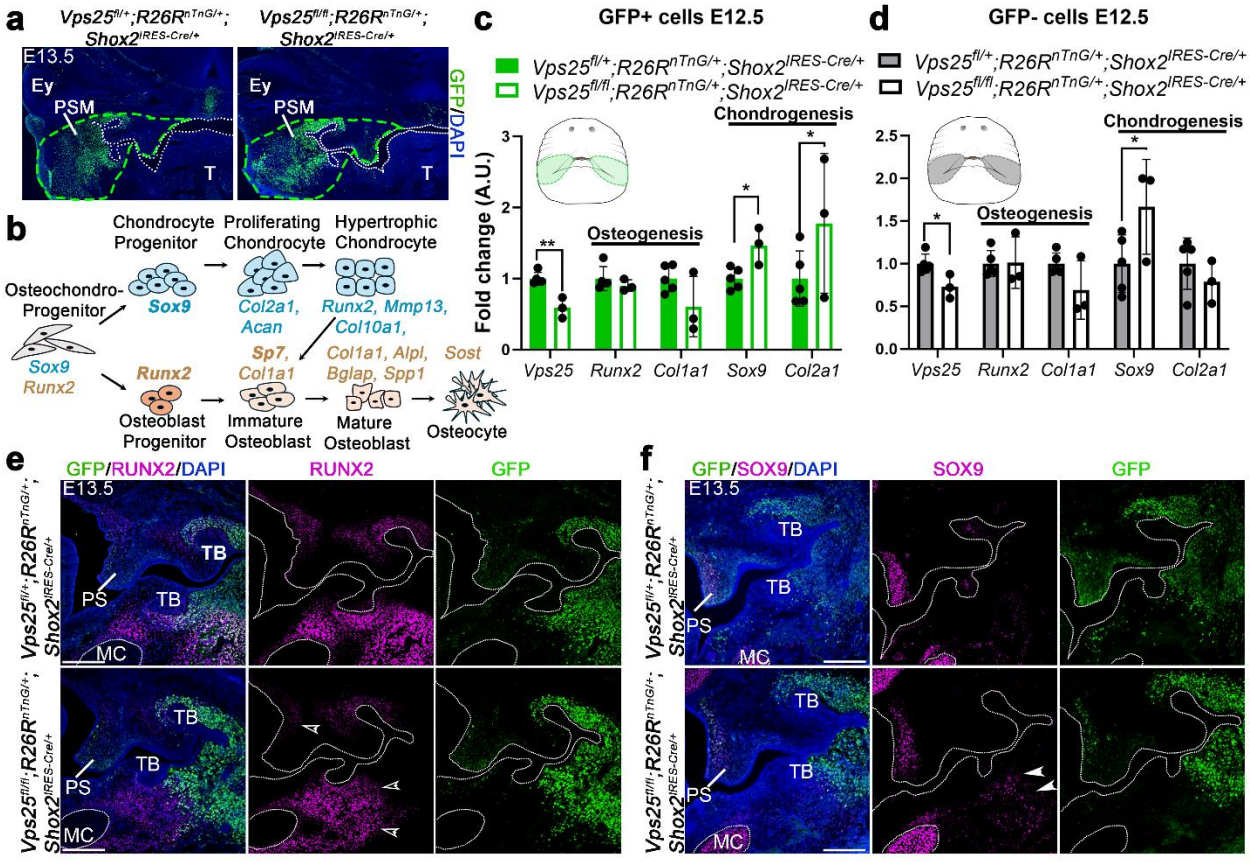


Figure 5. Perturbation of chondrogenic and osteogenic markers in VPS25-deficient craniofacial mesenchyme. (a) Visualization of GFP+ cells denoting Cre activity in PSM craniofacial tissue (dashed green line) from E13.5 heterozygous control (*Vps25$^{fl/+}$;R26R$^{nTnG/+}$;Shox2$^{IRES-Cre/+}$*, left) and homozygous mutant (*Vps25$^{fl/fl}$;R26R$^{nTnG/+}$;Shox2$^{IRES-Cre/+}$*, right) embryos. Ey; eye. T; tongue. **(b)** Schematic of osteo-chondroprogenitor differentiation highlighting specific markers for chondrogenic and osteogenic lineages. **(c,d)** Quantification of transcript levels for *Vps25,* chondrogenic (*Sox9, Col2a1*) and osteogenic (*Runx2, Col1a1*) markers in FACS purified GFP+ **(c)** and GFP- **(d)** cells from E12.5 heterozygous control and homozygous mutant PSM (shown in schematics). Increased expression of chondrogenic markers in *Vps25* homozygous mutant PSM. Error bars: SD. Multiple unpaired t-tests. p value ≤ 0.05=*; p value ≤ 0.01=**. **(e)** Decreased RUNX2+ domain (magenta, empty white arrowheads) in E13.5 mutant homozygous (*Vps25$^{fl/fl}$;R26R$^{nTnG/+}$;Shox2$^{IRES-Cre/+}$*) versus control heterozygous (*Vps25$^{fl/+}$;R26R$^{nTnG/+}$;Shox2$^{IRES-Cre/+}$*) PSM shown by immunofluorescence. GFP, *Cre* reporter, green. **(f)** Expanded domain of SOX9+ cells (magenta, white arrowheads) within and adjacent to Cre+ cells (GFP, green) in mutant embryos compared to heterozygous controls shown by immunofluorescence. DAPI: DNA, blue. PS; palatal shelves. MC; Meckel's cartilage. TB: tooth bud. Scale bar=200 µm. For panels **a**, **e**, and **f**, dotted white line outlines the oral cavity, tooth buds, and MC.

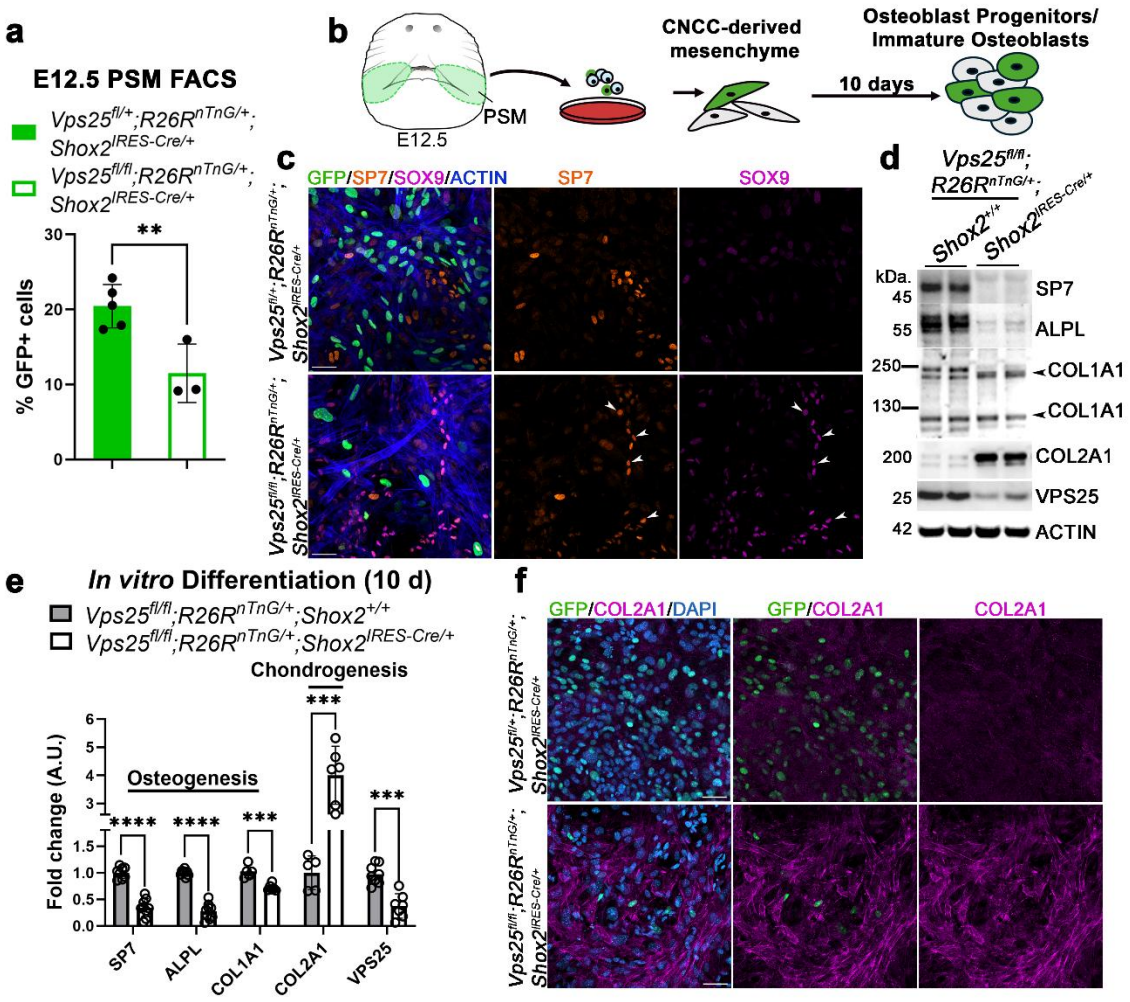


Figure 6. Chondrogenic markers persist upon osteogenic induction of *Vps25* mutant PSM cells. (a) Significantly lower percentage of *Cre*+/GFP+ cells in homozygous mutant (*Vps25$^{fl/fl}$;R26R$^{nTnG/+}$;Shox2$^{IRES-Cre/+}$*) compared to heterozygous (*Vps25$^{fl/+}$;R26R$^{nTnG/+}$;Shox2$^{IRES-Cre/+}$*) embryonic PSM, quantified by FACS. Error bars: SD. Unpaired t-test . p value ≤ 0.01=**. **(b)** Schematic of a 10-day in *vitro* osteogenic induction assay using PSM (green domains) cells from E12.5 *Vps25$^{fl/+}$;R26R$^{nTnG/+}$;Shox2$^{IRES-Cre/+}$* heterozygous control and *Vps25$^{fl/fl}$;R26R$^{nTnG/+}$;Shox2$^{IRES-Cre/+}$* mutant embryos. **(c)** Immunofluorescence of SP7 (orange), SOX9 (magenta), and GFP (green) in PSM cells cultured as shown in **(b)**. *Cre*+ cells visualized in green. Actin stained with phalloidin (blue). E12.5 mutant (*Vps25$^{fl/fl}$;R26R$^{nTnG/+}$;Shox2$^{IRES-Cre/+}$*, bottom) PSM cells remain SP7+ and SOX9+ (white arrowheads) during initial osteogenic induction, unlike control (*Vps25$^{fl/+}$;R26R$^{nTnG/+}$;Shox2$^{IRES-Cre/+}$*, top) cells. Scale bar =50 µm. **(d)** Lower levels of osteogenic proteins (SP7, COL1A1, and ALPL) and higher levels of the chondrogenic marker COL2A1 in cells from mutant PSM cultured as described in **(b),** shown by western blot. **(e)** Quantification of **(d)**, normalized to Actin. Error bars: SD. Multiple unpaired t-tests. p value ≤ 0.001=***; p value ≤ 0.0001=****. **(f)** Widespread increased COL2A1 (magenta) levels in cells from *Vps25* mutant *versus* control PSM confirmed by immunofluorescence. DAPI: DNA, blue. Scale bar =50 µm.

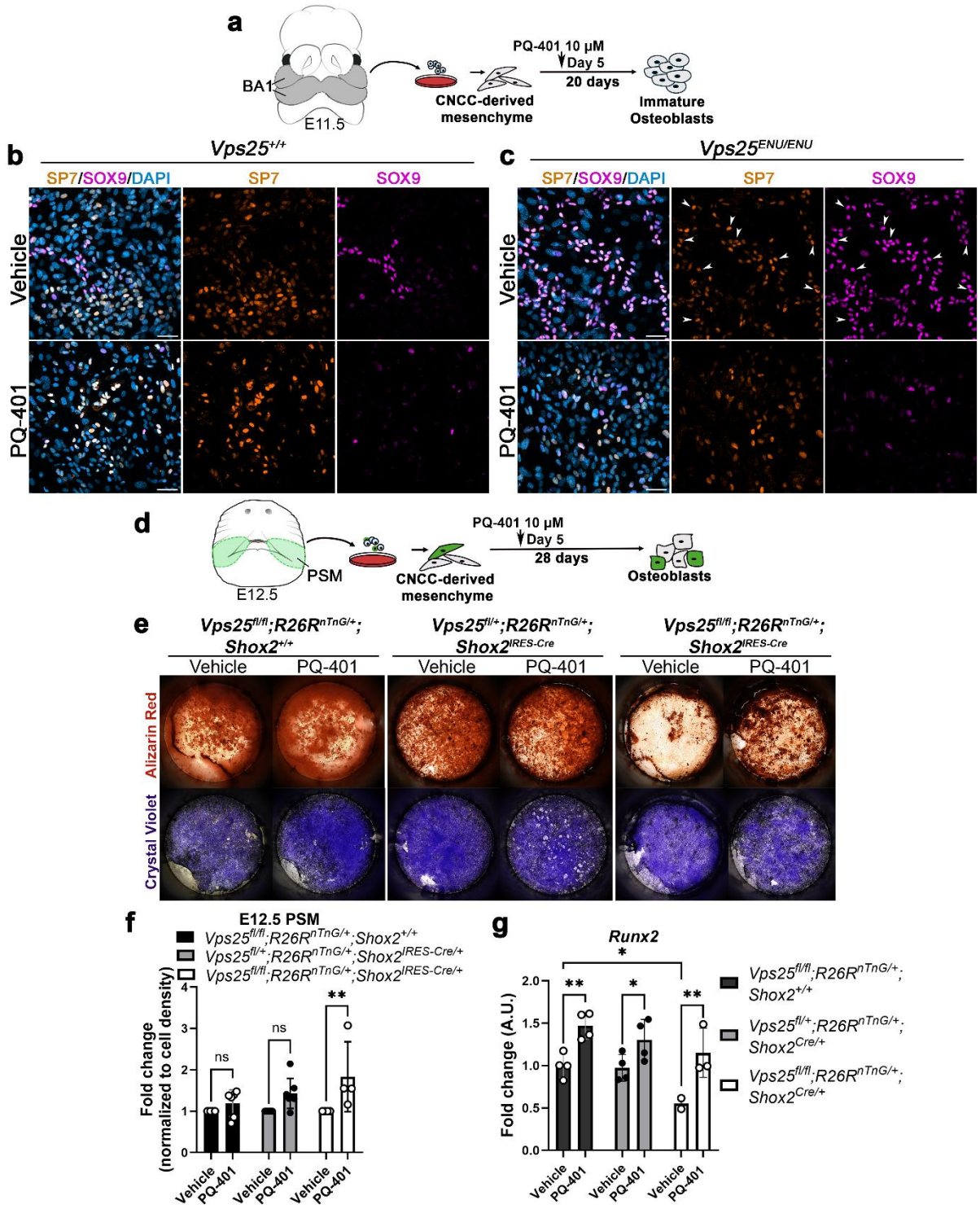


Figure 7. Dampening IGF signaling via inhibition of IGF1R rescues VPS25-dependent osteogenic differentiation. (a) Schematic of experimental strategy for a 20-day *in vitro* osteogenic induction assay of BA1 cranial neural crest cell (CNC)-derived mesenchymal cells. **(b,c)** Immunofluorescence of SP7 (orange) and SOX9 (magenta) in cells cultured as in **(a)**. **(b)** After 20 days of osteogenic induction, few SOX9-positive wildtype cells remained under either vehicle or PQ-401 treatment. **(c)** In contrast, mesenchymal cells from hypomorphic homozygous mutant *Vps25*$^{ENU/ENU}$ BA1 retained both SP7 and SOX9 (white arrowheads) after vehicle treatment. Following

IGF1R inhibition, the SOX9-positive population decreased in *Vps25* mutant cells. Scale bar=50 µm. **(d)** Schematic for *in vitro* differentiation of PSM cells into mature osteoblasts. **(e)** Alizarin red (top) and crystal violet (bottom) staining of *in vitro* differentiated PSM mesenchymal as in **(d)**. Decreased mineralization in cultured cells isolated from *Vps25* conditional homozygous mutant PSM compared to control PSM. Inhibition of IGF1R with PQ-401 restores, at least partly, mineralization in cell cultures from mutant embryos. **(f)** Quantification of alizarin red staining normalized to crystal violet intensity shown in **(e)**. Error bars: SD. Two-way ANOVA with Sidak's multiple comparisons test. p value ≤ 0.05=*; p value ≤ 0.01=**; ns= not significant. **(g)** *Runx2* transcript levels restored in PSM cells from *Vps25* conditional homozygous embryos after 10 days of osteogenic induction upon PQ-401 treatment, shown by qRT-PCR. Error bars=SD. Two-way ANOVA with Tukey's post-test. p value ≤ 0.05=*; p value ≤ 0.01=** .

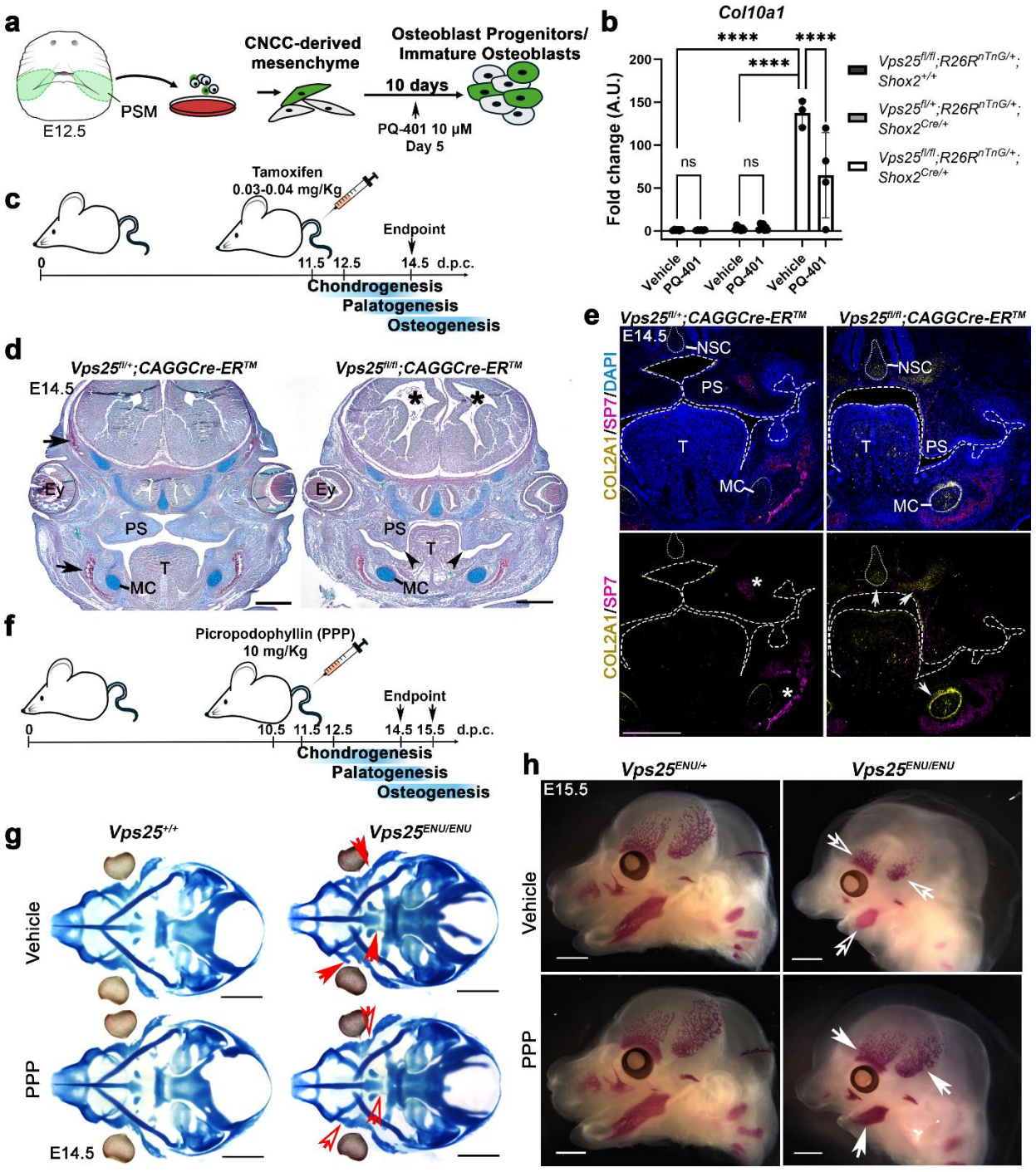


Figure 8. VPS25 loss leads to aberrant chondrogenic differentiation via upregulation of IGF1 signaling. (a) Schematic of 10-day in *vitro* osteogenic induction using PSM (green domains) cells obtained from E12.5 *Vps25*$^{fl/fl}$*;R26R*$^{nTnG/+}$*;Shox2*$^{+/+}$ *Cre* negative, *Vps25*$^{fl/+}$*;R26R*$^{nTnG/+}$*;Shox2*$^{IRES\text{-}Cre/+}$ heterozygous, and *Vps25*$^{fl/fl}$*;R26R*$^{nTnG/+}$*;Shox2*$^{IRES\text{-}Cre/+}$ homozygous mutant embryos. Vehicle (DMSO) or PQ-401 added on day 5. **(b)** Significantly increased levels of the hypertrophic marker gene *Col10a1* shown by qRT-PCR in cultured cells from *Vps25* homozygous mutant *versus* control embryos. Significant reduction of *Col10a1* transcripts in cells from homozygous mutant PSM upon PQ-401 treatment. Error bars=SD. Two-way ANOVA

with Tukey's post-test. p value ≤ 0.01=**; p value ≤ 0.001=***; p value ≤ 0.0001=****. **(c)** Schematic of tamoxifen-induced *Vps25* inactivation. Pregnant dams intraperitoneally injected with tamoxifen at 11.5 and 12.5 days post coitum (d.p.c.) to delete *Vps25* at the onset of chondrogenesis. **(d)** RGB-trichrome-stained coronal sections from E14.5 tamoxifen-induced controls and *Vps25* homozygous mutant embryos. Black arrows point to jaw and frontal bones stained with Sirius red (dark pink). Cleft palate (black arrowheads) and enlarged brain ventricles (black asterisks) in mutant compared to control embryos. Ey; eye. PS; palatal shelves. T; tongue. MC; Meckel's cartilage. Scale bar=500 µm. **(e)** Immunofluorescence showing chondrogenic marker COL2A1 accumulation (yellow, white arrows) and altered SP7 pattern (magenta, white asterisk) in tamoxifen-induced homozygous mutant PSM compared to controls. DAPI: DNA, blue. NSC; nasal septum cartilage (dotted white line). Dashed white line outlines oral cavity and tooth buds. Scale bar=500 µm. **(f)** Schematic of intraperitoneal injections with vehicle or the IGF1R inhibitor PPP to pregnant dams. **(g)** Upper view of E14.5 alcian blue-stained heads from wildtype and *Vps25*$^{ENU/ENU}$ mutant embryos from pregnant dams injected with vehicle (top) or PPP (bottom). Thinned cartilaginous structures (empty red arrows) in mutant embryos treated with PPP compared to cartilages (solid red arrows) from mutant embryos exposed to vehicle. Wildtype embryos remain unaffected. Scale bar=1 mm. **(h)** Lateral views of E15.5 alizarin red-stained heads from wildtype and *Vps25*$^{ENU/ENU}$ mutant embryos retrieved from pregnant dams treated as in **(f)**. PPP treatment results in expanded bone (solid white arrows) compared to mutant embryos treated with vehicle (empty white arrows). Scale bar=1 mm.

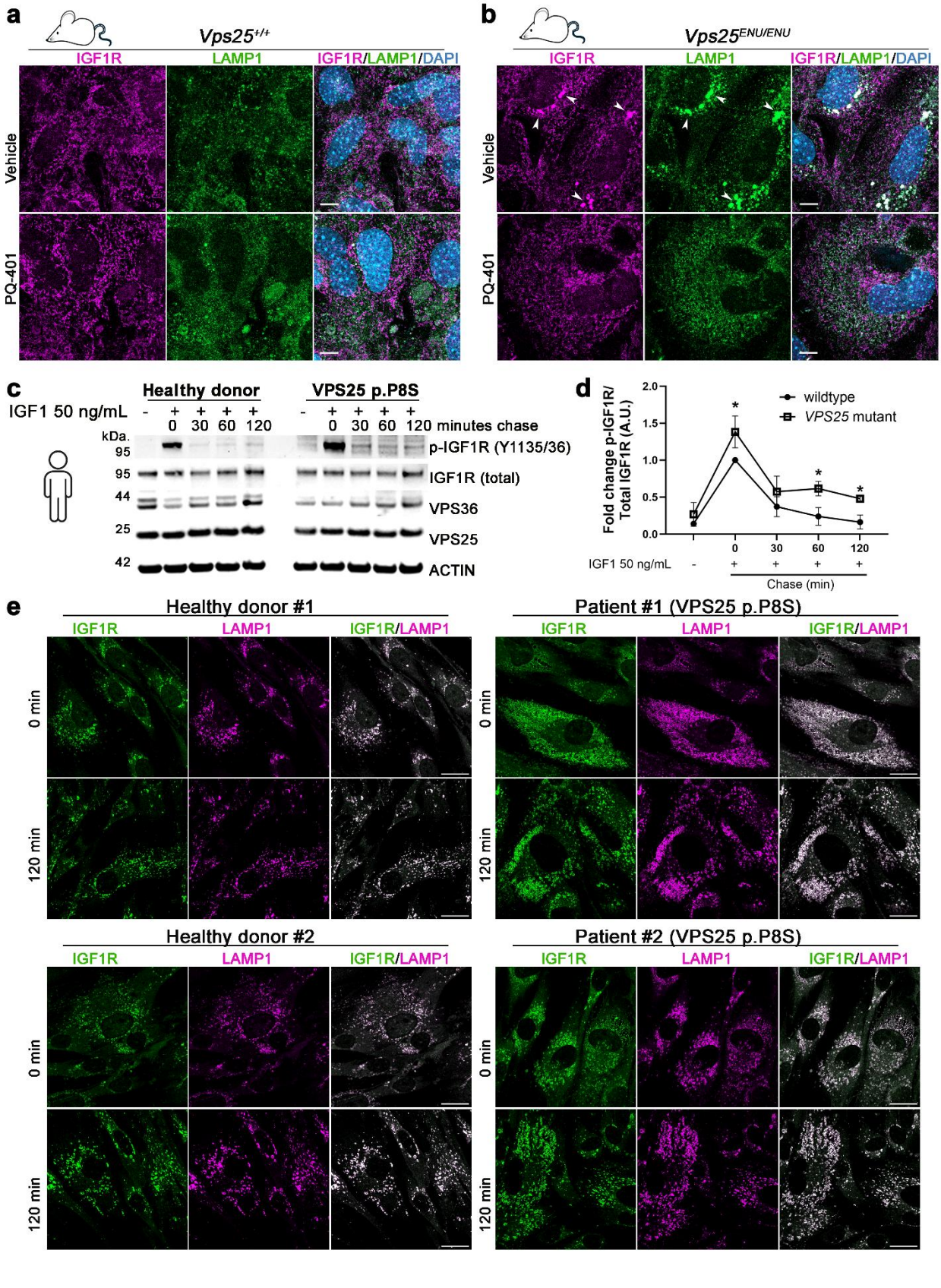

a
Vps25+/+
IGF1R
LAMP1
IGF1R/LAMP1/DAPI
Vehicle
PQ-401
b
Vps25ENU/ENU
IGF1R
LAMP1
IGF1R/LAMP1/DAPI
Vehicle
PQ-401
c
Healthy donor
VPS25 p.P8S
IGF1 50 ng/mL
- + + + + - + + + +
0 30 60 120 0 30 60 120 minutes chase
kDa.
95 p-IGF1R (Y1135/36)
95 IGF1R (total)
44 VPS36
25 VPS25
42 ACTIN
d
Fold change p-IGF1R/ Total IGF1R (A.U.)
2.0
1.5
1.0
0.5
0.0
wildtype
VPS25 mutant
*
0 30 60 120
IGF1 50 ng/mL - + + + +
Chase (min)
e
Healthy donor #1
Patient #1 (VPS25 p.P8S)
Healthy donor #2
Patient #2 (VPS25 p.P8S)
IGF1R
LAMP1
IGF1R/LAMP1
0 min
120 min

Figure 9. IGF1R is sequestered in endolysosomes in mouse and human *Vps25/VPS25*-mutant cells. (a, b) Immunofluorescence of IGF1R (magenta) and LAMP1 (green) in wildtype **(a)** and *Vps25* mutant **(b)** BA1 mesenchyme cells *in vitro* induced for 10 days into osteogenic lineage and treated with vehicle (DMSO) or PQ-401. IGF1R remains trapped and accumulates in engorged LAMP1+ compartments (white arrowheads) in vehicle-treated *Vps25* mutant cells **(b**, top**)**, unlike in wildtype cells **(a**, top**)**. Inhibition of IGF1R transphosphorylation prevents the receptor's intracellular accumulation in mutant cells **(b**, bottom**),** while its localization is not substantially affected by PQ-401 treatment in wildtype cells **(a**, bottom**)**. DAPI: DNA, blue. Scale bar=10 µm. **(c)** Immunoblot of activated IGF1R (p-IGF1R Y1135/36), total IGF1R, VPS36, VPS25, and Actin in fibroblasts from healthy donors (wildtype, left) and patients harboring *VPS25* mutations (right). Cells were untreated or exposed to IGF1 for 10 minutes and collected at the indicated timepoints. **(d)** Quantification of activated IGF1R, normalized to total IGF1R levels, in fibroblasts from three healthy donors and three different patients with biallelic *VPS25* mutations. Activated IGF1R accumulates in mutant cells after IGF1 treatment compared to control cells. Error bars: SD. Two-way ANOVA with Sidak's multiple comparisons test. p value ≤ 0.05=*. **(e)** Immunofluorescence showing IGF1R (green) localization to LAMP1+ (magenta) vesicles in MG-132-treated fibroblasts from healthy donors (left panels) and from patients carrying *VPS25* biallelic variants (right panels), at the indicated timepoints after IGF1 pulse. LAMP1+/IGF1R+ compartments are enlarged in cells with *VPS25* mutations compared to controls. Fibroblasts from two healthy donors and two patients carrying homozygous c.22C>T (p.Pro8Ser) variants are shown. Scale bar=20 µm.

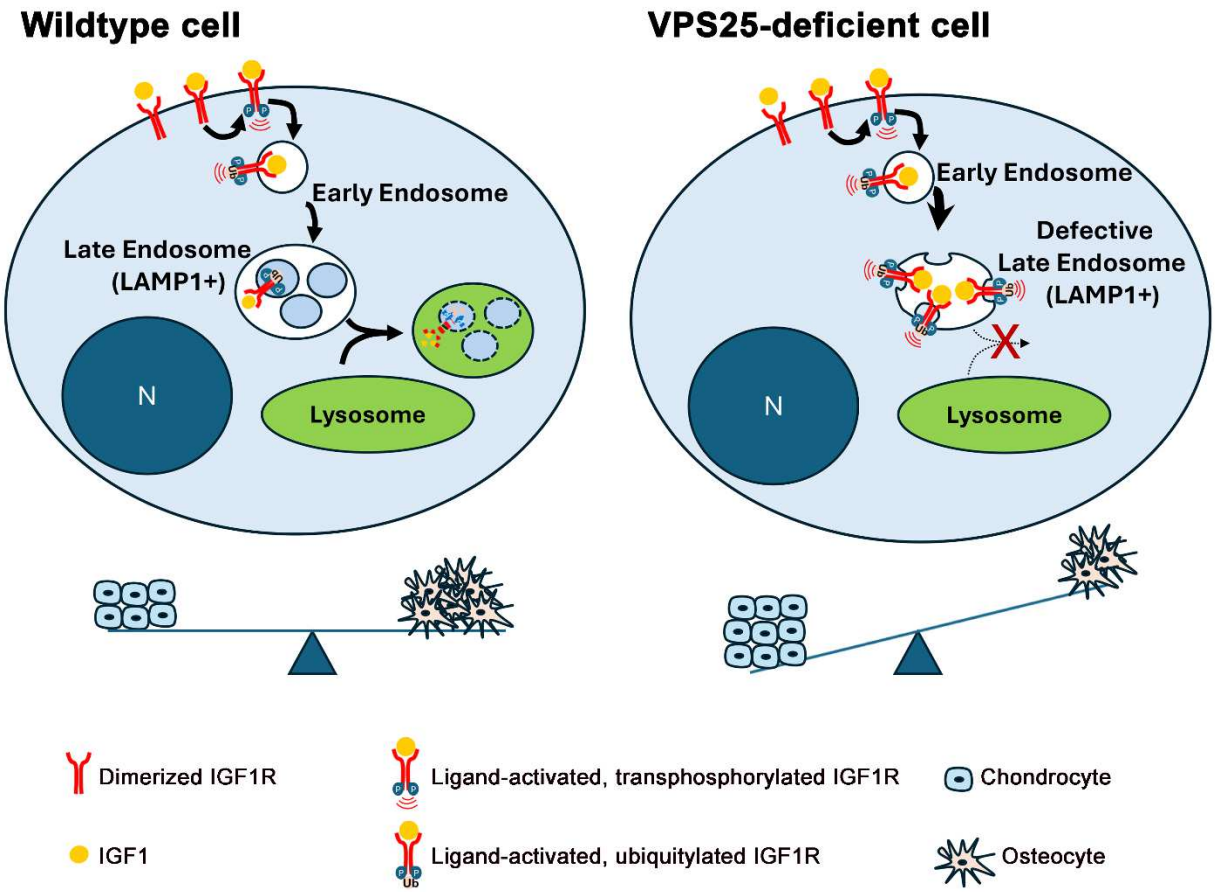
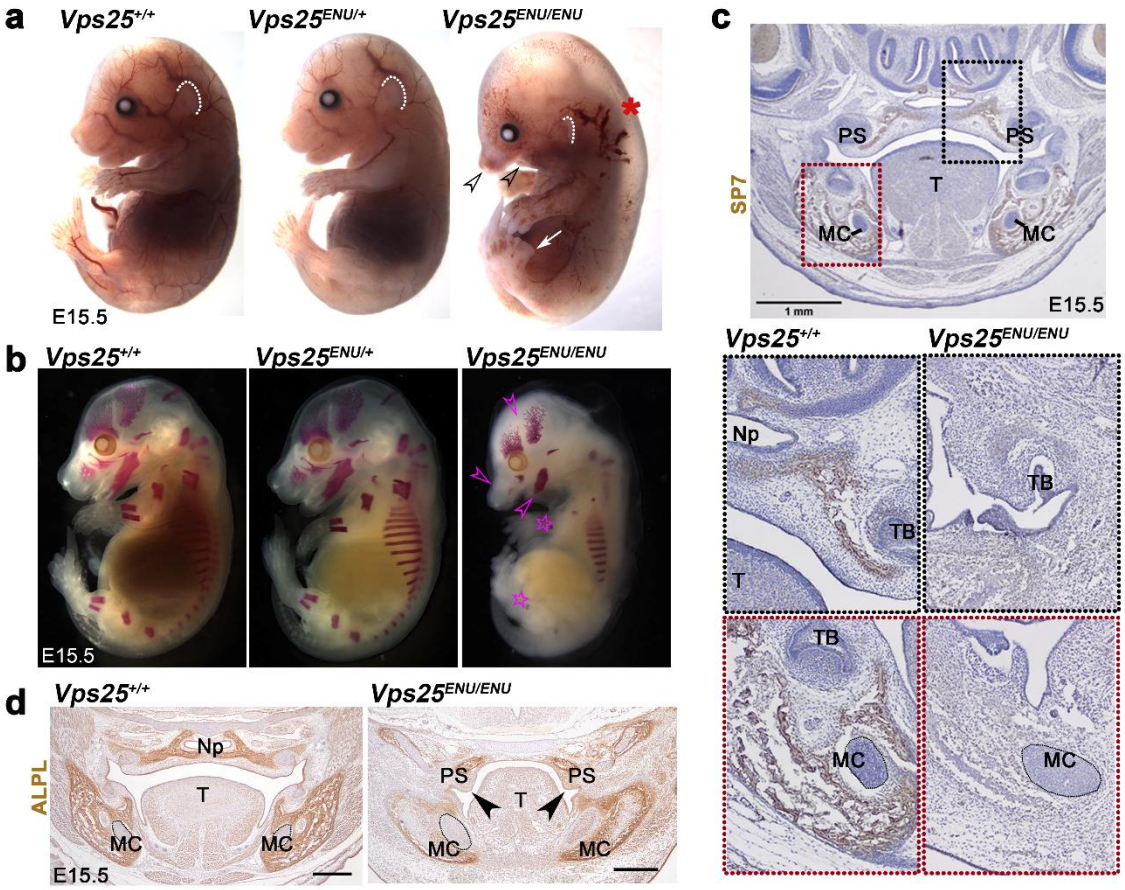
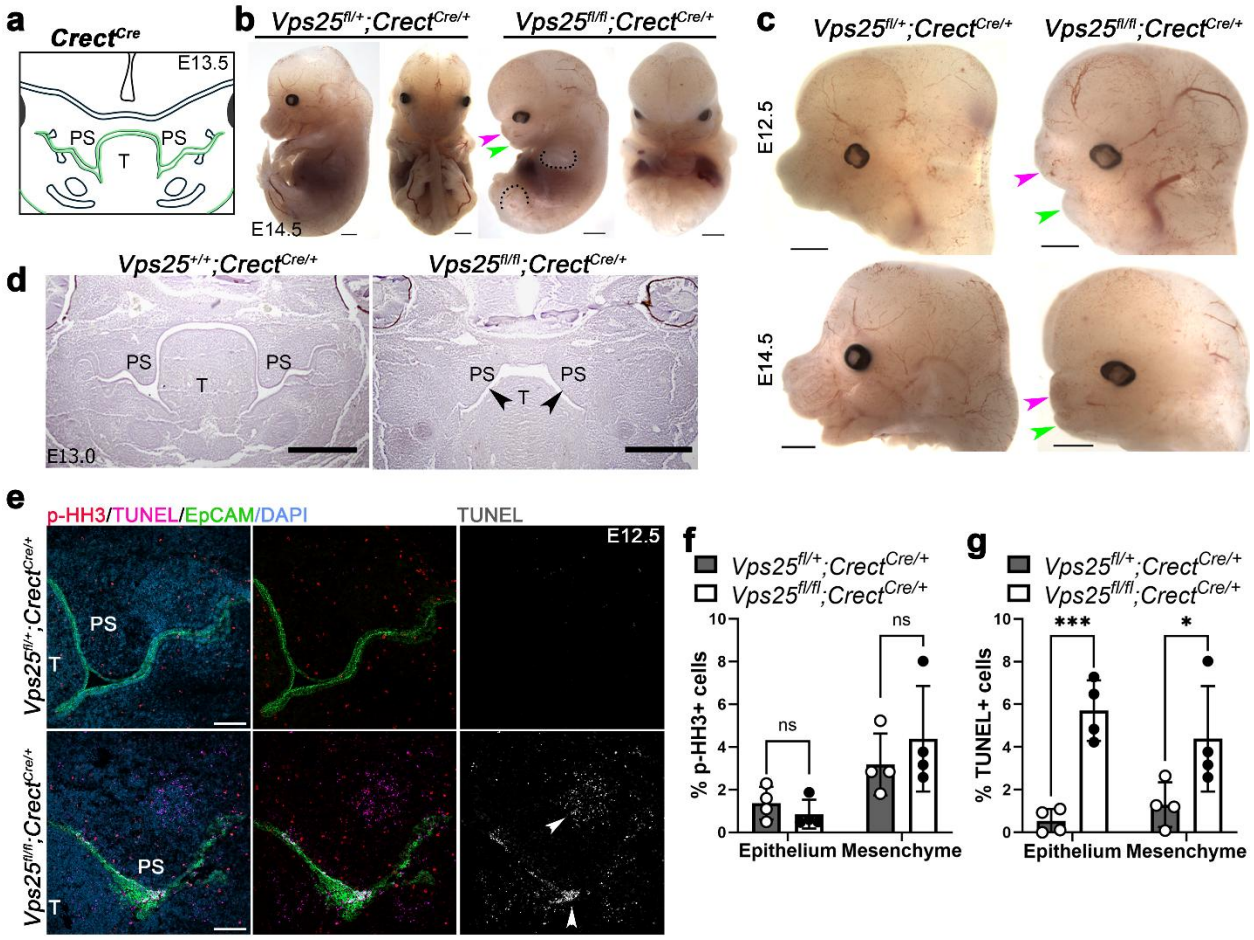


Figure 10. VPS25/ESCRT-II is required for IGF1R endo-lysosomal degradation during commitment/differentiation of osteochondroprogenitor cells into skeletal lineages. Model illustrating IGF1R trafficking in wildtype (left) and VPS25-deficient (right) cells. Upon ligand binding, IGF1R is internalized and sorted into late endosomes (LAMP+) for subsequent lysosomal degradation. When the ESCRT-II complex activity is compromised, IGF1R cannot be trafficked into lysosomes and remains trapped in late endosome-like (LAMP+) vesicles, while still signaling into the cytoplasm. This process is conserved in mice and humans. Accumulation of active IGF1R favors chondrogenic over osteogenic cell commitment/differentiation of murine osteochondroprogenitors. N; nucleus.

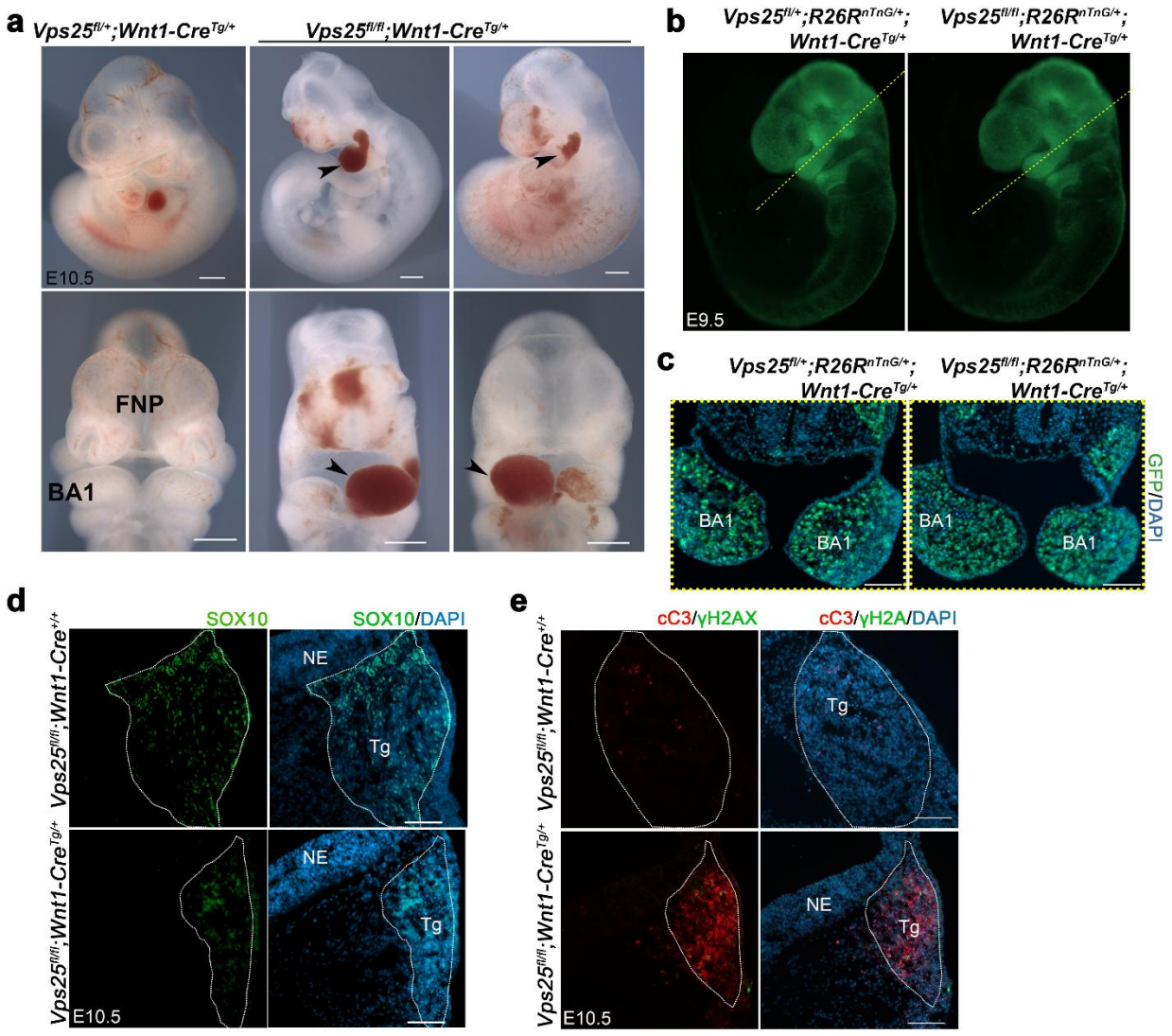


Supplementary figure 1. Impaired bone formation in *Vps25* hypomorphic mutants. **(a)** Gross morphology of *Vps25*$^{+/+}$, *Vps25*$^{ENU/+}$, and *Vps25*$^{ENU/ENU}$ embryos at E15.5. Empty arrowheads point to hypoplastic upper and lower jaw in a homozygous hypomorphic mutant embryo (*Vps25*$^{ENU/ENU}$). White arrow points to hindlimb polydactyly and red asterisk denotes edema in *Vps25*$^{ENU/ENU}$ mutant. Ear pinnae, hypoplastic and dysmorphic in mutant embryo, outlined by dotted white lines. **(b)** Alizarin red staining of embryos shown in **(a)** revealing hypoplastic calvarial as well as upper and lower jaw bones in *Vps25*$^{ENU/ENU}$ (empty magenta arrowheads) versus *Vps25*$^{+/+}$or *Vps25*$^{ENU/+}$ control embryos. Empty magenta stars show hypoplastic or absent long bones in mutant forelimbs and hindlimbs. **(c)** Top panel: SP7 immunohistochemistry in coronal sections comprising palatal shelves (PS), tooth bud (TB), and tongue (T) of E15.5 wildtype embryos, counterstained with hematoxylin. Black and dotted red rectangles depict inset areas of upper and lower jaw, respectively. High magnification insets of E15.5 wildtype and *Vps25*$^{ENU/ENU}$ embryos (bottom panels). Scale bar=1mm. **(d)** Coronal sections from E15.5 wildtype (*Vps25*$^{+/+}$) and mutant (*Vps25*$^{ENU/ENU}$) embryos show drastically decreased ALPL immunostaining in *Vps25* mutant embryo (right). Black arrowheads show defective PS elevation in *Vps25*$^{ENU/ENU}$ embryos. Scale bar=500 µm. Np: nasopharynx; MC; Meckel's cartilage (dotted black line).



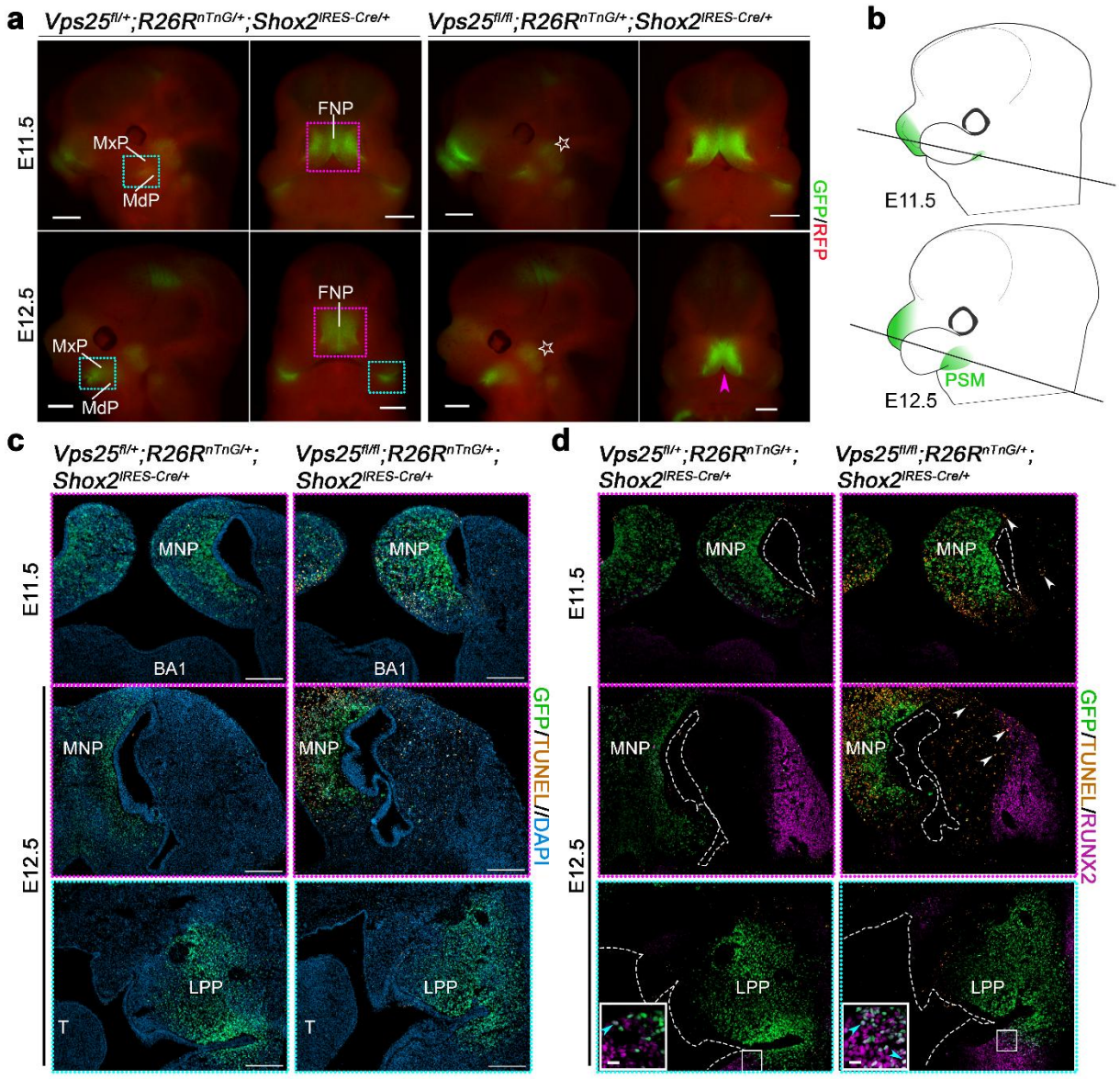
Supplementary figure 2. Loss of epithelial VPS25 leads to stunted jaw and hypoplastic palatal shelves. (a) Schematics of craniofacial tissues with Cre activity (green) in *Crect*^{Cre} embryos at E13.5. **(b)** Frontal and lateral views of E14.5 embryos with heterozygous (left panels) and homozygous (right panels) epithelial deletion of *Vps25* (*Vps25*$^{fl/+}$*;Crect*$^{Cre/+}$ and *Vps25*$^{fl/fl}$*;Crect*$^{Cre/+}$, respectively). Stunted snout (magenta arrowhead) and hypoplastic lower jaw (green arrowhead) in embryos with *Vps25* homozygous loss in cephalic epithelium compared to control embryos. Dotted black lines outline hypoplastic limbs in *Vps25*$^{fl/fl}$*;Crect*$^{Cre/+}$. Scale bar=1 mm. **(c)** Lateral views of *Vps25*$^{fl/+}$*;Crect*$^{Cre/+}$ control heterozygous and *Vps25*$^{fl/fl}$*;Crect*$^{Cre/+}$ homozygous heads at E12.5 (top panels) and E14.5 (bottom panels). Magenta arrowhead points to stunted snout; green arrowhead points to hypoplastic lower jaw in homozygous mutants versus control embryos. Scale bar=500 µm. **(d)** Hematoxylin staining of coronal sections from E13.0 control (*Vps25*$^{+/+}$*;Crect*$^{Cre/+}$) and mutant (*Vps25*$^{fl/fl}$*;Crect*$^{Cre/+}$) embryos. Black arrowheads point to mutant hypoplastic palatal shelves (PS). T; tongue. Scale bar=500 µm. **(e)** Immufluorescence of phosphorylated histone H3 on Ser10 (p-HH3, red) and EpCAM (green) with TUNEL (magenta or grey as indicated) and DAPI (blue) stainings in palatal tissue from E12.5 control (*Vps25*$^{fl/+}$*;Crect*$^{Cre/+}$, top panels) and mutant (*Vps25*$^{fl/fl}$*;Crect*$^{Cre/+}$, bottom panels) embryos. White arrowheads point to cell death in both mesenchyme and epithelium of mutant compared to control palatal tissue. Scale bar=100 µm. **(f,g)** Quantification of p-HH3+ **(f)** and TUNEL+ **(g)** cells in PS of

embryos shown in **(e)**. Error bars: SD. Two-way ANOVA with Šidák multiple comparisons test. p value ≤ 0.05=*; p value ≤ 0.001=***. ns=not significant.



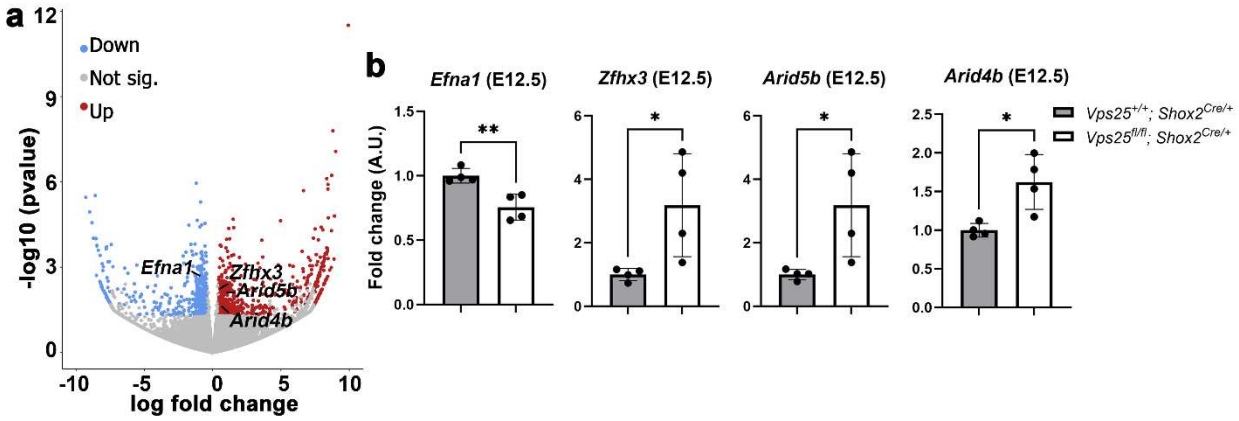
Supplementary figure 3. Mesenchymal VPS25 is critical for survival but not for migration of Cranial Neural Crest Cells (CNCCs). (a) lateral (top) and frontal (bottom) views of two embryos with homozygous deletion of *Vps25* in CNCCs (*Vps25$^{fl/fl}$;Wnt1-Cre$^{Tg/+}$*) and heterozygous control embryo (*Vps25$^{fl/+}$;Wnt1-Cre$^{Tg/+}$*) at E10.5. Arrows point to hemorrhage in branchial arch 1 (BA1) with CNCC-specific homozygous *Vps25* loss. FNP; frontonasal process. Scale bar=500 μm. **(b)** *Cre* reporter activity visualized by GFP signal (green) in embryos with heterozygous (*Vps25$^{fl/+}$;R26R$^{nTnG/+}$;Wnt1-Cre$^{Tg/+}$*) and homozygous (*Vps25$^{fl/fl}$;R26R$^{nTnG/+}$;Wnt1-Cre$^{Tg/+}$*) deletion of *Vps25* in CNCCs at E9.5. **(c)** GFP immunofluorescence in sections obtained as depicted by dotted yellow line shown in **(b)**. GFP+ cells migrate to and colonize BA1 in control (*Vps25$^{fl/+}$;R26R$^{nTnG/+}$;Wnt1-Cre$^{Tg/+}$*) and homozygous mutant (*Vps25$^{fl/fl}$;R26R$^{nTnG/+}$;Wnt1-Cre$^{Tg/+}$*) embryos. DAPI: DNA, blue. Scale bar=100 μm. **(d)** SOX10 (green) immunofluorescence in transverse sections of *Vps25$^{fl/fl}$;Wnt1-Cre$^{+/+}$* control (top panels) and *Vps25$^{fl/fl}$;Wnt1-Cre$^{Tg/+}$* mutant (bottom panels) embryos at E10.5. Dashed white line delineates the area of SOX10+ cells from the trigeminal migratory stream (Tg). DAPI: DNA, blue. NE; neuroepithelium. Scale bar=100 μm. **(e)** Immunofluorescence of

cleaved Caspase 3 (cC3, apoptotic cell death, red) and histone H2AX phosphorylated at Ser139 (γH2AX, genomic instability, green) in transverse sections of control (*Vps25*$^{fl/fl}$*;Wnt1-Cre*$^{+/+}$) and mutant (*Vps25*$^{fl/fl}$*;Wnt1-Cre*$^{Tg/+}$) embryos at E10.5. Dashed white line envelops the cells from the trigeminal migratory stream. DAPI: DNA, blue. Scale bar=100 μm.

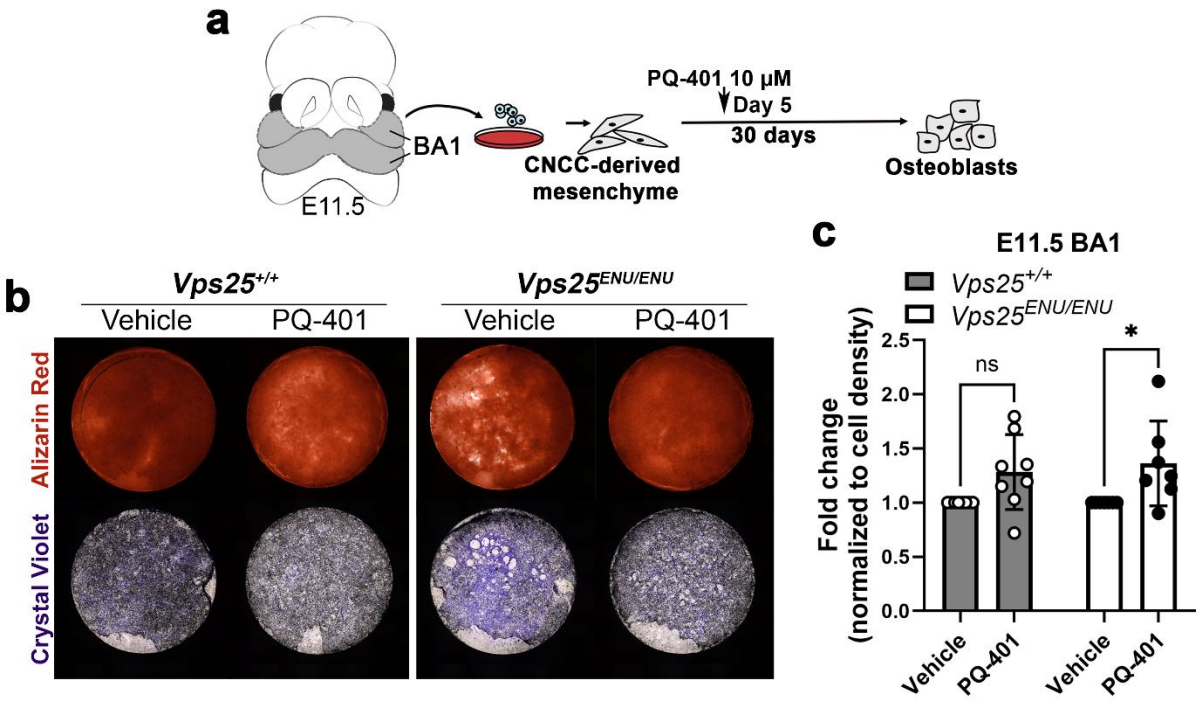


Supplementary figure 4. Identification of *Vps25*-deficient cellular populations in craniofacial prominences. (a) *Cre* reporter activity visualized by GFP signal (green) at the junction between the maxillary (MxP) and mandibular (MdP) prominences (dotted cyan square) and in the frontonasal prominence (FNP) at the midline (dotted magenta square) in *Vps25*$^{fl/+}$;*R26R*$^{nTnG/+}$; *Shox2*$^{IRES\text{-}Cre/+}$ control and *Vps25*$^{fl/fl}$;*R26R*$^{nTnG/+}$;*Shox2*$^{IRES\text{-}Cre/+}$ mutant embryos at E11.5 (top) and E12.5 (bottom). Magenta arrowhead points to facial clefting in *Vps25* mutant embryos at E12.5. White star denotes cranial ganglion. Scale bar=1 mm. **(b)** Schematic of craniofacial prominences displaying Cre activity (green) at E11.5 (top) and E12.5 (bottom). **(c-d)** Immunofluorescence of GFP (green) and RUNX2 (magenta), as well as TUNEL staining (orange), in transverse sections, obtained as shown in **b**, from conditional heterozygous controls and homozygous mutant embryos. *Vps25*-deficient, GFP^{+}, Cre^{+} cells (green) observed in the medial nasal prominence (MNP) at E11.5 (**c** and **d** top panels) and at E12.5 (**c** and **d** middle panels). White arrowheads point to TUNEL^{+}, GFP^{-} cells (**d**, top and middle panels). GFP^{+} cells are present in the lateral palatal process (LPP) at E12.5

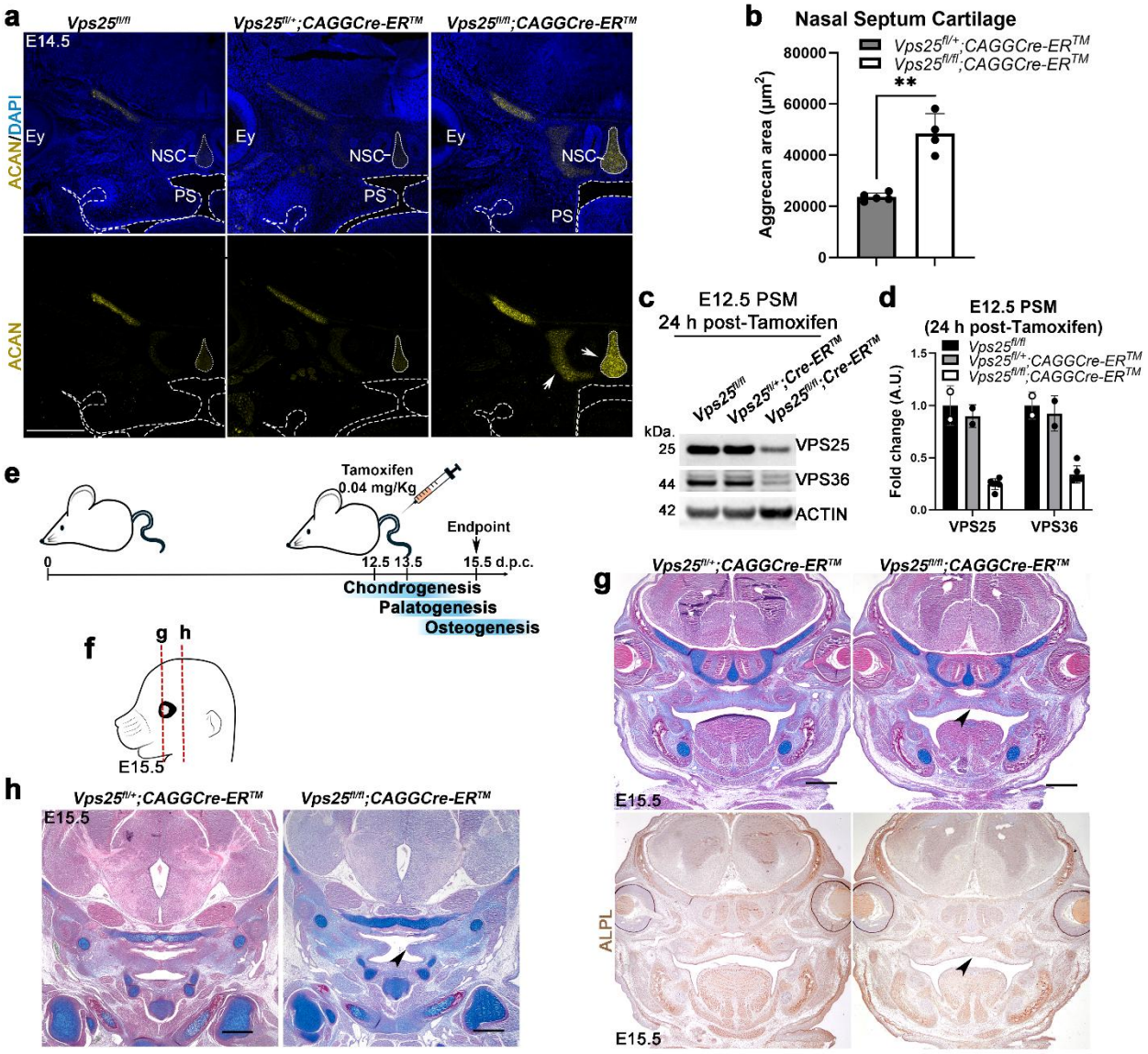
(**c** and **d**, bottom panels). Cyan arrowheads in magnified inset (**d**, bottom panel) show GFP^{+},RUNX2^{+} cells at E12.5. T; tongue. Scale bar=200 µm. Inset bar=20 µm.



Supplementary figure 5. Validation of dysregulated genes in *Vps25*-deficient craniofacial mesenchyme. (a) volcano plot generated from datasets of differentially expressed genes (DEGs) in *Vps25$^{fl/fl}$;Shox2$^{IRES\text{-}Cre/+}$ versus Vps25$^{+/+}$;Shox2$^{IRES\text{-}Cre/+}$* PSM tissue, obtained by RNA-Seq. Red and blue dots depict significantly up and down regulated genes, respectively. Highlighted DEGs encode signaling molecules (E*fna1*) or genes previously associated with craniofacial defects. **(b)** Quantification of DEG transcript levels in mutant *versus* control PSM tissue at E12.5 by qRT-PCR. Error bars: SD. Unpaired t-test. p value ≤ 0.01=**; p value ≤ 0.05=*.



Supplementary figure 6. Pharmacological IGF1R inhibition rescues defective *in vitro* osteogenic differentiation of *Vps25* hypomorphic cells. (a) Schematic of *in vitro* differentiation of BA1 cells into mature osteoblasts. Vehicle or PQ-401 added on day 5 of induction. **(b)** Alizarin red (top) and crystal violet (bottom) staining of BA1 cells treated as in (**a**). Decreased mineralization in cultured cells isolated from *Vps25* hypomorphic BA1 (*Vps25*$^{ENU/ENU}$) shown by alizarin red intensity compared to wildtype cells. IGF1R pharmacological inhibition with PQ-401 rescues the mutant mineralization phenotype. **(c)** Quantification of alizarin red staining normalized to crystal violet intensity shown in **(b)**. Error bars: SD. Two-way ANOVA with Sidak's multiple comparisons test. p value ≤ 0.05=*; p value ≤ 0.01=**; ns= not significant.



Supplementary figure 7. Abnormal skeletal phenotype is established prior to osteogenesis in *Vps25* mutants. (a) Immunofluorescence showing increased area and intensity of the chondrogenic marker Aggrecan (ACAN, yellow, white arrows) in *Vps25* homozygous mutants exposed to tamoxifen at E11.5, compared to tamoxifen-treated controls. DAPI: DNA, blue. Ey; eye. NSC; nasal septum cartilage (dotted white line). PS; palatal shelves. Dashed white line outlines oral cavity and tooth buds. Scale bar=500 µm. **(b)** Quantification of ACAN+ NSC area in heterozygous and homozygous tamoxifen-induced *Vps25* embryos shown in **(a)**. Error bars: SD. Unpaired t-test . p value ≤ 0.01=**. **(c)** Immunoblot of ESCRT-II subunits VPS25 and VPS36, as well as Actin, in e12.5 PSM tissue from homozygous tamoxifen-induced *Vps25*-deficient and controls embryos, 24 hours after first tamoxifen injection at E11.5. **(d)** Quantification of **(c)**, normalized to Actin. Error bars: SD. **(e)** Schematic of later tamoxifen-induced inactivation of *Vps25* using a *CAGGCre-ER^{TM}* deleter line. Pregnant dams were intraperitoneally injected with 0.04 mg/Kg of tamoxifen at 12.5 and 13.5 days post coitum (d.p.c.). **(f)** Schematic of anterior and mid palatal coronal sections from embryos retrieved from tamoxifen-treated dams shown in **(e)**. **(g)** Similar morphology of mid

palatal coronal sections from E15.5 tamoxifen-induced heterozygous control and homozygous mutant embryos stained with RGB-trichrome (top). Dark magenta (sirius red) denotes developing bone. Blue (alcian blue) highlights cartilage. Black arrowhead points to modest secondary palatal thinning in *Vps25* homozygous mutant embryos. ALPL immunohistochemistry with hematoxylin counterstain (bottom) in tamoxifen-induced heterozygous controls and homozygous mutant embryos. Scale bar=500 μm**.** **(h)** Cleft of the posterior secondary palate (black arrowhead) in E15.5 *Vps25* homozygous mutant embryos compared to heterozygous controls, shown by RGB-trichrome staining. Scale bar=500 μm.

Supplementary Table 1: Genotyping primers

Line	Orientation	5'->3' Sequence
Vps25^{ENU}	Forward	GGAGGGGGCTAGATCATTCT
	Reverse	TGTGTCTTAAGAGAGCAATGGTG
Vps25^{flox}	Forward	GGCTACTACGATGGCGATGAGTTTC
	Reverse	GACTTAAAGACCCCAGCACTCATTAACTA
Cre (general)	Forward	GTTCGCAAGAACCTGATGGACA
	Reverse	CTAGAGCCTGTTTTGCACGTTC
CAGGCre	Forward	AGGTGGACCTGATCATGGAG
	Reverse	ATACCGGAGATCATGCAAGC
	Internal Control Forward	CTAGGCCACAGAATTGAAAGATCT
	Internal Control Reverse	CTAGGCCACAGAATTGAAAGATCT
R26R^{nTnG}	Forward	GGAGCGGGAGAAATGGATATG
	Reverse	AAAGTCGCTCTGAGTTGTTAT
	Reverse_Mut	CCAGGCGGGCCATTTACCGTA AG

Supplementary Table 2: qPCR primers

Gene	Orientation	5'->3' Sequence
Vps25	Forward	**TCATTTACCAATGGGTTTCC**
	Reverse	**TCTGTGTCTTCCCCACTCG**
Runx2_3'	Forward	**TCCTCTCTCAGTAAGAAGAGCC**
	Reverse	**ATGAAATGCTTGGGAACTGCC**
Runx2_5'	Forward	**AACGATCTGAGATTTGTGGGC**
	Reverse	**AATAGCTCTGTGGTAAGTGGCC**
Cdh1	Forward	**CAGGTCTCCTCATGGCTTTGC**
	Reverse	**CTTCCGAAAAGAAGGCTGTCC**
Epcam	Forward	**GCGGCTCAGAGAGACTGTG**
	Reverse	**CCAAGCATTTAGACGCCAGTTT**
Hand2	Forward	**AAGGACGACCAGAACGGAGA**
	Reverse	**GTTGCTGCTCACTGTGCTTT**
Plod3	Forward	**TCTCTCTTCCTTCACAACAGC**
	Reverse	**ACAGCTGAAAAATGGTCCTGG**
Alpl	Forward	**AATTCATACTGCATGTCCCCG**
	Reverse	**CAAGCATTCCCACTATGTCTGG**
Sox9	Forward	**CAAGACTCTGGGCAAGCTCT**
	Reverse	**GTGGTCTTTCTTGTGCTGCA**
Igf1r	Forward	**TGACTCGGATGGCTTCGTTA**
	Reverse	**TTTCTTCTCTTCATCGCCGC**
Col2a1	Forward	**AGGTGTTCGAGGAGACAGTG**
	Reverse	**CAACAATGCCCCTTTGACCA**
Col1a1	Forward	**GTTCAGCTTTGTGGACCTCC**
	Reverse	**TTTCCACGTCTCACCATTGG**
Col10a1	Forward	**ATGCTGAACGGTACCAAACG**
	Reverse	**GGAATGCCTTGTTCTCCTCT**
Efna1	Forward	**GCCACATCGTCTTCTGGAAC**
	Reverse	**TCCTCGTAATGTGGGCAGAT**
Zfhx3	Forward	**CAGTCAGGCAGAGAAGGAGT**
	Reverse	**GCTCGGGTTTGATCTCCTCT**

Arid5b	Forward	**TTTCCTCCCCGAAGACACTC**
	Reverse	**GCCCATTTGACAAGGTCCTC**
Arid4b	Forward	**GAGCCTTCTGTGAAGCCAAG**
	Reverse	**AGTGGGCCCTTTATGTGGTC**
Gak	Forward	**GCTGTCTACAACCTTTCTCCAAG**
	Reverse	**ATGCACAACACAGACGTTCCT**
Tbp	Forward	**CTATCACTCCTGCCACACCA**
	Reverse	**CAGTTGTCCGTGGCTCTCTT**
Rpl13	Forward	**CCCTCCACCCTATGACAAGA**
	Reverse	**GTAGGCTTCAGCCGAACAAC**

Supplementary Files

This is a list of supplementary files associated with this preprint. Click to download.

- Supplfig4.tif
- Suppl.table2.pdf
- supplfig5.tif
- supplfig7.tif
- Suppl.table1.pdf
- supplFig.6.tif
- supplfig2.tif
- Supplfig1.tif
- Supplfig3.tif
- UNCROPPEDWESTERNBLOTS.xlsx